Structure of cold nuclear matter at subnuclear densities by Quantum Molecular Dynamics

Gentaro Watanabe[a,b], Katsuhiko Sato[a,c], Kenji Yasuoka[d] and Toshikazu Ebisuzaki[b]
[a] *Department of Physics, University of Tokyo, Tokyo 113-0033, Japan*
[b] *Division of Computational Science, RIKEN, Saitama 351-0198, Japan*
[c] *Research Center for the Early Universe, University of Tokyo, Tokyo 113-0033, Japan*
[d] *Department of Mechanical Engineering, Keio University, Yokohama 223-8522, Japan*
(Dated: February 8, 2008)

Structure of cold nuclear matter at subnuclear densities for the proton fraction $x = 0.5$, 0.3 and 0.1 is investigated by quantum molecular dynamics (QMD) simulations. We demonstrate that the phases with slablike and rodlike nuclei, etc. can be formed dynamically from hot uniform nuclear matter without any assumptions on nuclear shape, and also systematically analyze the structure of cold matter using two-point correlation functions and Minkowski functionals. In our simulations, we also observe intermediate phases, which has complicated nuclear shapes. It is found out that these phases can be characterized as those with negative Euler characteristic. Our result implies the existence of these kinds of phases in addition to the simple "pasta" phases in neutron star crusts and supernova inner cores.

In addition, we investigate the properties of the effective QMD interaction used in the present work to examine the validity of our results. The resultant energy per nucleon ϵ_n of the pure neutron matter, the proton chemical $\mu_p^{(0)}$ in pure neutron matter and the nuclear surface tension $E_{\rm surf}$ are generally reasonable in comparison with other nuclear interactions.

PACS numbers: 21.65.+f,26.50.+x,26.60.+c,61.20.Ja

arXiv:nucl-th/0308007v1 2 Aug 2003

I. INTRODUCTION

For the past several decades since the discovery of pulsars, many authors have investigated the properties of dense matter which exist inside neutron stars and supernova cores (see, e.g., Refs. [1, 2, 3]). These objects have been shown that they consist of a variety of material phases whose physical properties reflect in many astrophysical phenomena of these objects. Especially, the properties of nuclear matter under extreme conditions, which is one of the essential topics for understanding the mechanism of collapse-driven supernovae [4], the structure of neutron star crusts [5] and its relating phenomena, have been studied actively. This subject is also interesting as one of the fundamental problems of the complex fluids of nucleons.

At subnuclear densities, nuclear matter exhibits the coexistence of a liquid phase with a gas phase due to the internucleon interaction which has an attractive part. At sufficiently low temperatures relevant to neutron star interiors, and sufficiently below the normal nuclear density, long-range Coulomb interactions make the system divide periodically into gas and spherical liquid drops, adding a crystalline property to the liquid-gas coexistence.

In the density region where nuclei are about to melt into uniform matter, it is expected that the energetically favorable configuration of the mixed phase possesses interesting spatial structures such as rodlike and slablike nuclei and rodlike and spherical bubbles, etc., which are referred to as nuclear "pasta". This picture was originally proposed by Ravenhall et al. [6] and Hashimoto et al. [7] independently. Their predictions both based on free energy calculations with liquid drop models assuming some specific nuclear shapes. These works clarify that the most energetically stable nuclear shape is determined by a subtle balance between the nuclear surface and Coulomb energies. Detailed aspects of equilibrium phase diagrams, such as a series of nuclear shapes which can be realized as the energetically most favorable and the density range corresponding to the phases with nonspherical nuclei, vary with nuclear models [8]. However, the realization of the "pasta" phases as energy minimum states can be seen in a wide range of nuclear models and the phase diagrams possess an universal basic feature that, with increasing density, the shape of the nuclear matter region changes like sphere → cylinder → slab → cylindrical hole → spherical hole → uniform [9, 10]. This feature is also reproduced by the Thomas-Fermi calculations by several groups [11, 12, 13].

The phases with these exotic nuclear structures, if they were realized in neutron star crusts or supernova cores, bring about many astrophysical consequences. As for those in neutron star phenomena, it is interesting to note the relevance of nonspherical nuclei to pulsar glitches and cooling of neutron stars. Although the question whether the mechanism of pulsar glitches is depicted by vortex pinning model or star quake model has yet to be settled completely, the existence of nonspherical nuclei in neutron star matter (NSM) have significant effects in both cases. As for the former, while the force needed to pin vortices has yet to be clarified completely even for a bcc lattice of spherical nuclei mainly due to the uncertain properties of impurities and defects [14], the effect of spatial structure of normal nuclear matter on vortex dynamics cannot be ignored. As for the latter, the existence of "pasta" phases with slablike and rodlike

nuclei would change the elastic properties of inner crust matter from those of crystalline solid to those of liquid crystal as indicated by Pethick and Potekhin [15], which results in significant decrease of the maximum elastic energy that can be stored in the inner crust. The presence of nonspherical nuclei would also accelerate the cooling of the corresponding region of neutron stars by opening semileptonic weak processes which are unlikely to occur for spherical nuclei [8].

"Pasta" phases in supernova matter (SNM) are expected to affect the neutrino transport and hydrodynamics in supernova cores. Let us first note that the neutrino wavelengths, typically of order 20 fm, are comparable to or even greater than the internuclear spacing, leading to diffractive effects on the neutrino elastic scattering off such a periodic spatial structure of nuclear matter [6]. These effects, induced by the internuclear Coulombic correlations, would reduce the scattering rates and hence the lepton fraction Y_L. For the bcc lattice of spherical nuclei, such a reduction was examined by Horowitz [16] by calculating the associated static structure factor. It is also noteworthy that nonspherical nuclei and bubbles are elongated in specific direction. In such direction, the neutrino scattering processes are no longer coherent, in contrast to the case of roughly spherical nuclei whose finiteness in any direction yields constructive interference in the scattering. The final point to be mentioned is that the changes in the nuclear shape are accompanied by discontinuities in the adiabatic index, denoting how hard the equation of state of the material is. These discontinuities may influence the core hydrodynamics during the initial phase of the collapse [12].

Though the properties of "pasta" phases in equilibrium state have been investigated actively, the formation and the melting processes of these phases have not been discussed except for some limited cases which are based on perturbative approaches [5, 17]. It is important to adopt a microscopic and dynamical approach which allows arbitrary nuclear structures in order to understand these processes of nonspherical nuclei. At finite temperatures, it is considered that not only nuclear surface becomes obscure but also nuclei of various shapes may coexist. Therefore, it is necessary to incorporate density fluctuations without any assumptions on nuclear shape to investigate the properties of "pasta" phases at finite temperatures. Although the works done by Williams and Koonin [11] and Lassaut et al. [12] do not assume nuclear structure, they can not incorporate fluctuations of nucleon distributions in a satisfying level because they are based on the Thomas-Fermi calculation, which is one-body approximation. In addition, only a single structure is contained in the simulation box in these works, there are thus possibilities that nuclear shape is strongly affected by boundary effect and some structures are prohibited implicitly.

In the present work, we study the structure of cold dense matter at subnuclear densities in the framework of quantum molecular dynamics (QMD) [18], which is one of the molecular dynamics (MD) approaches for nucleon many-body systems (see, e.g., Ref. [19] for review). MD for nucleons including QMD, which is a microscopic and dynamical method without any assumptions on nuclear structure, is suitable for incorporating fluctuations of particle distributions. Previously, we have reported the first results of our study on nuclear "pasta" by QMD, which demonstrated that the "pasta" phases can be formed in a dynamical way for matter with proton fractions $x = 0.3$ and 0.5 [20]. In this full paper, we present new results for astrophysically interesting neutron-rich matter of $x = 0.1$ in addition to the cases of $x = 0.3$ and 0.5 reported before.

The plan of this paper is as follows. In Section II, we describe the framework of the QMD model used in the present study. We then show the results of our simulations in Section III and analyze the structure of matter obtained by the simulations using two-point correlation functions and Minkowski functionals in Section IV. In Section V, we investigate the properties of the effective nuclear interaction used in this work in order to examine the validity of our results in terms of nuclear forces. Astrophysical discussions are given in Section VI. Summary and conclusions are presented in Section VII.

II. QUANTUM MOLECULAR DYNAMICS

We have various types of molecular dynamics methods for nucleons including representative ones such as fermionic molecular dynamics (FMD) [21], antisymmetrized molecular dynamics (AMD) [22] and QMD, etc. In the present work, we choose QMD among them balancing between calculation cost and accuracy. The typical length scale l of inter-structure is $l \sim 10$ fm and the density region of interest is just below the normal nuclear density $\rho_0 = 0.165$ fm^{-3}. The required nucleon number N in order to reproduce n unit structures in the simulation box is about $N \sim \rho_0(nl)^3$ (for slabs). It is thus desirable that we prepare nucleons of order 10000 if we try to reduce boundary effects down to a satisfactory level by reproducing several several unit structures in the box. While it is a hard task to treat such a large system with, for example, FMD and AMD whose calculation costs scale as $\sim N^4$, it is feasible to do it with QMD whose calculation costs scale as $\sim N^2$. This difference comes from summations in the Slater determinants in the trial wave functions of the former models. In QMD, on the other hand, the total N-nucleon wave function $|\Phi\rangle$ is assumed to be a direct product of single-nucleon states $|\phi_i\rangle$:

$$|\Phi\rangle = |\phi_1\rangle \otimes |\phi_2\rangle \otimes \cdots \otimes |\phi_N\rangle \ . \tag{1}$$

The single-nucleon state is represented by a Gaussian wave packet:

$$\phi_i(\mathbf{r}) = \langle \mathbf{r}|\phi_i\rangle = \frac{1}{(2\pi L)^{3/4}} \exp\left[-\frac{(\mathbf{r}-\mathbf{R}_i)^2}{4L} + \frac{i}{\hbar}\ \mathbf{r}\cdot\mathbf{P}_i\right], \tag{2}$$

where $\mathbf{R}_i(t)$ and $\mathbf{P}_i(t)$ are the centers of position and momentum of the packet i, respectively, and L is a parameter related to the extension of the wave packet in the coordinate space.

It is also noted that we mainly focus on the macroscopic structures; the exchange effect would not be so important for them. This can be seen by comparing the typical values of the exchange energy for the macroscopic scale and of the energy difference between two successive phases with nonspherical nuclei. Suppose there are two identical nucleons, $i = 1$ and 2, bound in different nuclei each other. The exchange energy between these particles is calculated as an exchange integral:

$$K = \int U(\mathbf{r}_1 - \mathbf{r}_2)\ \varphi_1(\mathbf{r}_1)\varphi_1^*(\mathbf{r}_2)\varphi_2(\mathbf{r}_2)\varphi_2^*(\mathbf{r}_1)\ d\mathbf{r}_1 d\mathbf{r}_2\ , \tag{3}$$

where U is the potential energy. An asymptotic form of the wave function is given by

$$\varphi_i \sim \exp\left(-\kappa_i r\right)\ , \tag{4}$$

with $r = |\mathbf{r}_1 - \mathbf{r}_2|$ and $\kappa_i = \frac{1}{\hbar}\sqrt{2mE_i}$, $(i = 1, 2)$, where E_i is the binding energy and m is the nucleon mass. The exchange integral reads

$$K \sim \exp\left[-(\kappa_1 + \kappa_2)R\right] \sim 5 \times 10^{-6}\mathrm{MeV} \tag{5}$$

for the internuclear distance $R \simeq 10$ fm and $E_i \simeq 8$ MeV, which is extremely smaller than the typical energy difference per nucleon between the "pasta" phases of order 0.1 keV (for NSM, see Fig. 4 in Ref. [9]) - 10 keV (for SNM, see Fig. 4 in Ref. [10]). Therefore, it is expected that QMD, which is less elaborate in treating the exchange effect, is not bad approximation for investigating the nuclear "pasta". Consequently, QMD has the advantages over the other models in the present study. In the future, we will have to confirm the validity of the results obtained by QMD using other more elaborate model such as AMD or FMD to treat the exchange effect more precicely. However, this problem is beyond the scope of the present work.

A. Model Hamiltonian

To simulate nuclear matter at subnuclear densities within the framework of QMD, we use a QMD model Hamiltonian developed by Maruyama et al. [23], which is constructed so as to reproduce bulk properties of nuclear matter and properties of finite nuclei. This model Hamiltonian consists of the following six terms

$$\mathcal{H} = T + V_{\mathrm{Pauli}} + V_{\mathrm{Skyrme}} + V_{\mathrm{sym}} + V_{\mathrm{MD}} + V_{\mathrm{Coulomb}}\ , \tag{6}$$

where T is the kinetic energy, V_{Pauli} is the Pauli potential introduced to reproduce the Pauli principle effectively, V_{Skyrme} is the Skyrme potential which consists of an attractive two-body term and a repulsive three-body term, V_{sym} is the symmetry potential, V_{MD} is the momentum-dependent potential introduced as two Fock terms of the Yukawa interaction and V_{Coulomb} is the Coulomb potential. The expressions of these terms are given as

$$T = \sum_{i,j(\neq i)} \frac{\mathbf{P}_i^{\mathbf{2}}}{2m_i}\ , \tag{7}$$

$$V_{\mathrm{Pauli}} = \frac{1}{2}\ C_{\mathrm{P}} \left(\frac{\hbar}{q_0 p_0}\right)^3 \sum_{i,j(\neq i)} \exp\left[-\frac{(\mathbf{R}_i - \mathbf{R}_j)^2}{2q_0^2} - \frac{(\mathbf{P}_i - \mathbf{P}_j)^2}{2p_0^2}\right] \delta_{\tau_i\tau_j}\delta_{\sigma_i\sigma_j}\ , \tag{8}$$

$$V_{\mathrm{Skyrme}} = \frac{\alpha}{2\rho_0} \sum_{i,j(\neq i)} \rho_{ij} + \frac{\beta}{(1+\tau)\ \rho_0^{\tau}} \sum_i \left[\sum_{j(\neq i)} \int d^3\mathbf{r}\ \tilde{\rho}_i(\mathbf{r})\ \tilde{\rho}_j(\mathbf{r})\right]^{\tau}\ , \tag{9}$$

$$V_{\mathrm{sym}} = \frac{C_{\mathrm{s}}}{2\rho_0} \sum_{i,j(\neq i)} \left(1 - 2|c_i - c_j|\right)\ \rho_{ij}\ , \tag{10}$$

$$\begin{aligned} V_{\mathrm{MD}} &= V_{\mathrm{MD}}^{(1)} + V_{\mathrm{MD}}^{(2)} \\ &= \frac{C_{\mathrm{ex}}^{(1)}}{2\rho_0} \sum_{i,j(\neq i)} \frac{1}{1 + \left[\frac{\mathbf{P}_i - \mathbf{P}_j}{\hbar\mu_1}\right]^2}\ \rho_{ij} + \frac{C_{\mathrm{ex}}^{(2)}}{2\rho_0} \sum_{i,j(\neq i)} \frac{1}{1 + \left[\frac{\mathbf{P}_i - \mathbf{P}_j}{\hbar\mu_2}\right]^2}\ \rho_{ij}\ , \end{aligned} \tag{11}$$

$$V_{\mathrm{Coulomb}} = \frac{e^2}{2} \sum_{i,j(\neq i)} \left(\tau_i + \frac{1}{2}\right)\left(\tau_j + \frac{1}{2}\right) \iint d^3\mathbf{r}\, d^3\mathbf{r}' \frac{1}{|\mathbf{r} - \mathbf{r}'|}\ \rho_i(\mathbf{r})\rho_j(\mathbf{r}')\ , \tag{12}$$

where ρ_{ij} means the overlap between the single-nucleon densities, $\rho_i(\mathbf{r})$ and $\rho_j(\mathbf{r})$, for i-th and j-th nucleons given as

$$\rho_{ij} \equiv \int d^3\mathbf{r}\ \rho_i(\mathbf{r})\ \rho_j(\mathbf{r})\ , \tag{13}$$

σ_i is the nucleon spin and τ_i is the isospin ($\tau_i = 1/2$ for protons and $-1/2$ for neutrons) and $C_{\rm P}$, q_0, p_0, α, β, τ, $C_{\rm s}$, $C_{\rm ex}^{(1)}$, $C_{\rm ex}^{(2)}$, μ_1, μ_2 and L are model parameters determined to reproduce the properties of the ground states of the finite nuclei, especially heavier ones, and the saturation properties of nuclear matter [23]. A parameter set used in this work is shown in Table I. The single-nucleon densities $\rho_i(\mathbf{r})$ and $\tilde{\rho}_i(\mathbf{r})$ are given by

$$\rho_i(\mathbf{r}) = |\phi_i(\mathbf{r})|^2 = \frac{1}{(2\pi L)^{3/2}} \exp\left[-\frac{(\mathbf{r}-\mathbf{R}_i)^2}{2L}\right], \quad (14)$$

$$\tilde{\rho}_i(\mathbf{r}) = \frac{1}{(2\pi \tilde{L})^{3/2}} \exp\left[-\frac{(\mathbf{r}-\mathbf{R}_i)^2}{2\tilde{L}}\right], \quad (15)$$

with

$$\tilde{L} = \frac{(1+\tau)^{1/\tau}}{2} L . \quad (16)$$

The modified width $\tilde{L}$ in $\tilde{\rho}_i(\mathbf{r})$ is introduced in the three-body term of Skyrme interaction [Eq. (9)] to incorporate the effect of the repulsive density-dependent term.

TABLE I: Effective interaction parameter set (incompressibility K=280 MeV; medium EOS model in Ref. [23])

$C_{\rm P}$ (MeV)	207
p_0 (MeV/c)	120
q_0 (fm)	1.644
α (MeV)	−92.86
β (MeV)	169.28
τ	1.33333
$C_{\rm s}$ (MeV)	25.0
$C_{\rm ex}^{(1)}$ (MeV)	−258.54
$C_{\rm ex}^{(2)}$ (MeV)	375.6
μ_1 (fm^{-1})	2.35
μ_2 (fm^{-1})	0.4
L (fm^2)	2.1

We adopt QMD equations of motion with friction terms to simulate the dynamical relaxation:

$$\begin{aligned} \dot{\mathbf{R}}_i &= \frac{\partial \mathcal{H}}{\partial \mathbf{P}_i} - \xi_R \frac{\partial \mathcal{H}}{\partial \mathbf{R}_i} , \\ \dot{\mathbf{P}}_i &= -\frac{\partial \mathcal{H}}{\partial \mathbf{R}_i} - \xi_P \frac{\partial \mathcal{H}}{\partial \mathbf{P}_i} , \end{aligned} \quad (17)$$

where the friction coefficients ξ_R and ξ_P are positive definite, which determine the relaxation time scale. The relaxation scheme given by Eqs. (17) is referred to as the steepest descent method and it leads to the continuous decrease in $\mathcal{H}$ as

$$\begin{aligned} \frac{d\mathcal{H}}{dt} &= \dot{\mathbf{R}}_i \cdot \frac{\partial \mathcal{H}}{\partial \mathbf{R}_i} + \dot{\mathbf{P}}_i \cdot \frac{\partial \mathcal{H}}{\partial \mathbf{P}_i} \\ &= -\xi_R \left(\frac{\partial \mathcal{H}}{\partial \mathbf{R}_i}\right)^2 - \xi_P \left(\frac{\partial \mathcal{H}}{\partial \mathbf{P}_i}\right)^2 \le 0 . \end{aligned} \quad (18)$$

Even though it is recognized that this method is not efficient, it is expected that the dynamics given by Eqs. (17) with $\xi_R, \xi_P \ll 1$ deviates slightly in a short period from the physically grounded dynamics given by QMD equations of motion without the friction terms [equations without the second terms in the right-hand sides of Eqs. (17)], which we would like to respect.

III. QMD SIMULATIONS OF COLD MATTER AT SUBNUCLEAR DENSITIES

A. QMD Simulations for $x = 0.5$ and 0.3

We have performed QMD simulations of an infinite (n, p, e) system with fixed proton fractions $x = 0.5$ and 0.3 for various nucleon densities ρ [the density region is (0.05 - 1.0) ρ_0]. We set 2048 nucleons (1372 nucleons in some cases) contained in a cubic box which is imposed by the periodic boundary condition. Throughout this paper, the numbers of the protons (neutrons) with up-spin and with down-spin are equal. The relativistic degenerate electrons which ensure the charge neutrality are regarded as a uniform background and the Coulomb interaction is calculated by the Ewald method taking account of the Gaussian charge distribution of each wave-packet (see Appendix A). This method enables us to efficiently sum up contributions of long-range interactions in a system with periodic boundary conditions. For nuclear interaction, we use the effective Hamiltonian developed by Maruyama et al. (medium EOS model) [23] whose expressions are given in the last Section.

We first prepare an uniform hot nucleon gas at $k_B T \sim 20$ MeV as an initial condition equilibrated for $\sim 500 - 2000$ fm/c in advance. In order to realize the ground state of matter, we then cool it down slowly for $O(10^3 - 10^4)$ fm/c, keeping the nucleon density constant with the frictional relaxation method [Eqs. (17)], etc. [24] until the temperature gets ~ 0.1 MeV or less. Note that no artificial fluctuations are given in the simulation.

The QMD equations of motion with the friction terms given by Eqs. (17) are solved using the fourth-order Gear predictor-corrector method in conjunction with multiple time step algorithm [26]. Integration time steps Δt are set to be adaptive in the range of $\Delta t < 0.1 - 0.2$ fm/c depending on the degree of convergence. At each step, the correcting operation is iterated until the error of position Δr and the relative error of momentum $\Delta p/p$ become smaller than 10^{-6}, where Δr and $\Delta p/p$ are estimated as the maximum values of correction among all particles. We mainly use PCs(Pentium III) equipped with MDGRAPE-2, which accelerates calculations of momentum-independent forces including the long-range Coulomb force.

Shown in Figs. 1 and 2 are the resultant nucleon dis-

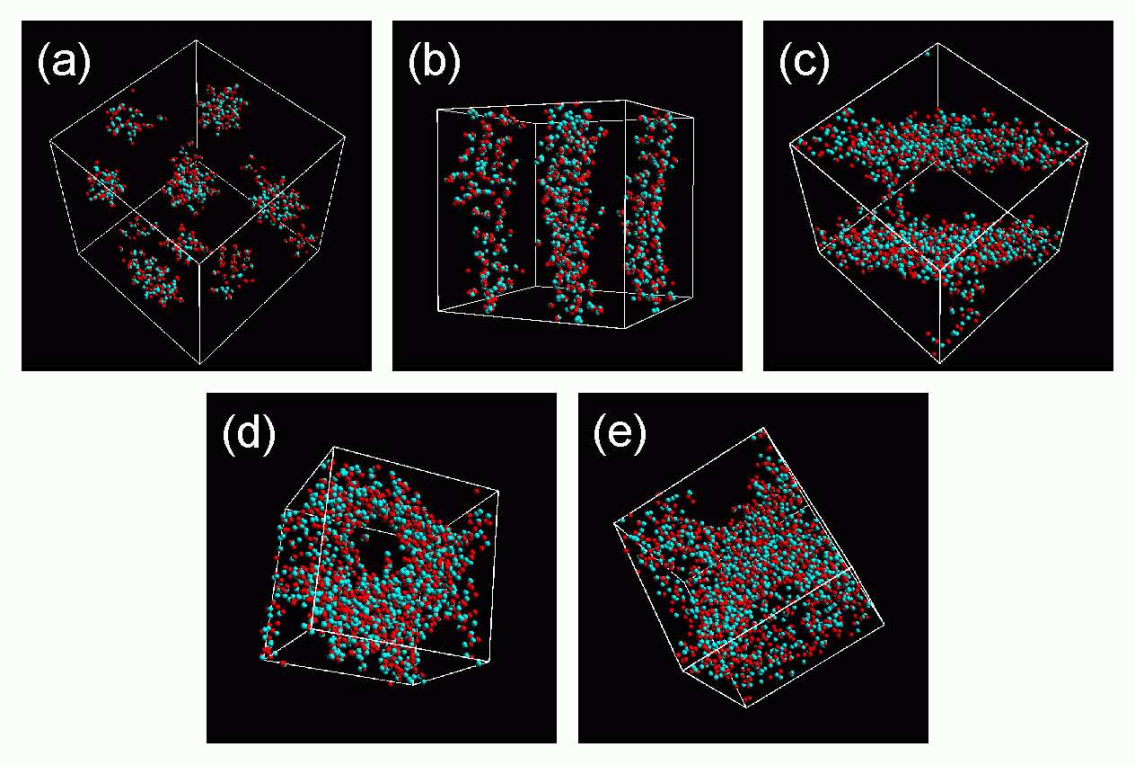

FIG. 1: (Color) The nucleon distributions of typical phases with simple structures of cold matter at $x = 0.5$; (a) sphere phase, $0.1\rho_0$ ($L_{\rm box} = 43.65$ fm, $N = 1372$); (b) cylinder phase, $0.225\rho_0$ ($L_{\rm box} = 38.07$ fm, $N = 2048$); (c) slab phase, $0.4\rho_0$ ($L_{\rm box} = 31.42$ fm, $N = 2048$); (d) cylindrical hole phase, $0.5\rho_0$ ($L_{\rm box} = 29.17$ fm, $N = 2048$) and (e) spherical hole phase, $0.6\rho_0$ ($L_{\rm box} = 27.45$ fm, $N = 2048$), where $L_{\rm box}$ is the box size. The red particles represent protons and the green ones represent neutrons.

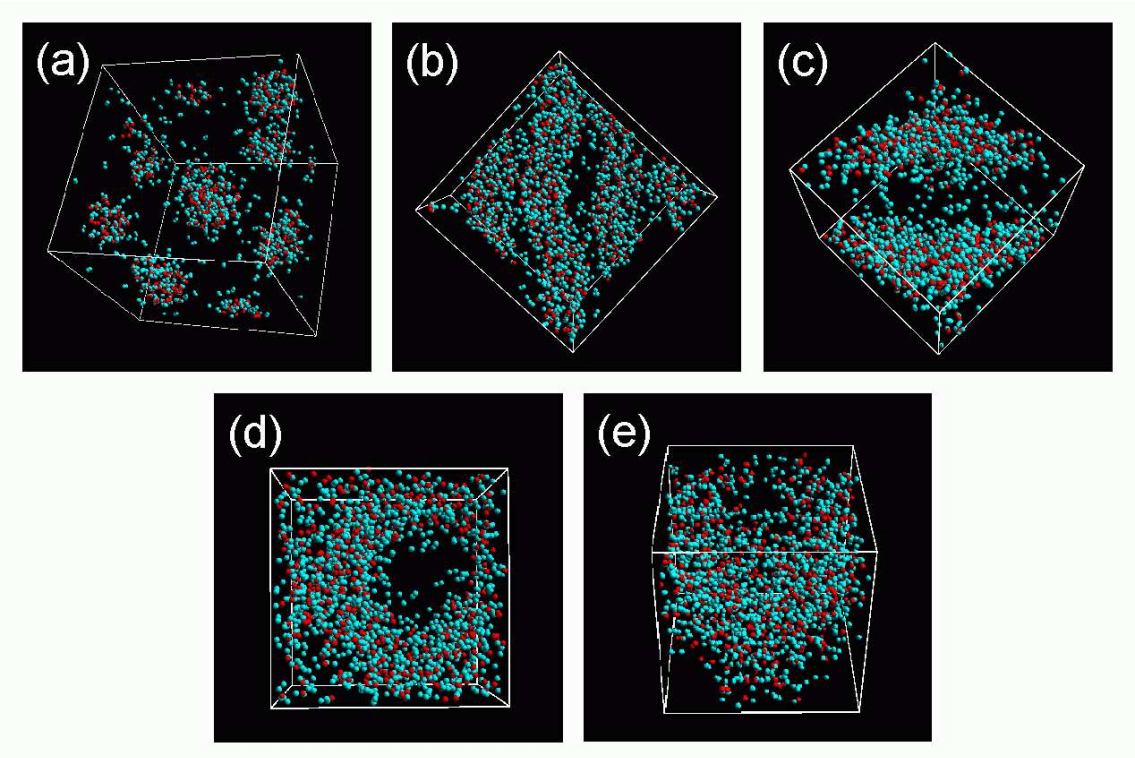

FIG. 2: (Color) Same as Fig. 1 at $x = 0.3$; (a) sphere phase, $0.1\rho_0$ ($L_{\rm box} = 49.88$ fm, $N = 2048$); (b) cylinder phase, $0.18\rho_0$ ($L_{\rm box} = 41.01$ fm, $N = 2048$); (c) slab phase, $0.35\rho_0$ ($L_{\rm box} = 32.85$ fm, $N = 2048$); (d) cylindrical hole phase, $0.5\rho_0$ ($L_{\rm box} = 29.17$ fm, $N = 2048$) and (e) spherical hole phase, $0.55\rho_0$ ($L_{\rm box} = 28.26$ fm, $N = 2048$). The red particles represent protons and the green ones represent neutrons.

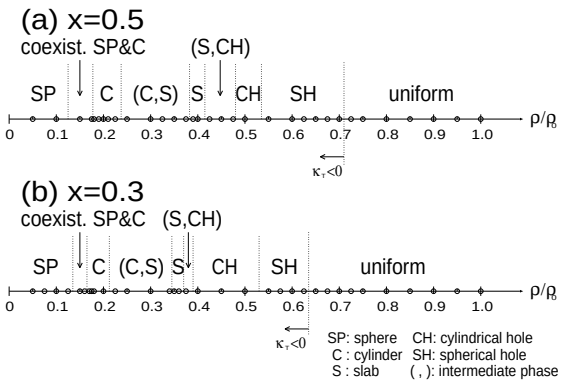

FIG. 3: Phase diagrams of cold matter at $x = 0.5$ (a) and $x = 0.3$ (b). Matter is unstable against phase separation in the density region shown as $\kappa_T < 0$, where κ_T is the isothermal compressibility. The symbols SP, C, S, CH and SH stand for nuclear shapes, i.e., sphere, cylinder, slab, cylindrical hole and spherical hole, respectively. The parentheses (A,B) show intermediate phases between A-phase and B-phase suggested in this work. They have complicated structures different from those of both A-phase and B-phase. Simulations have been carried out at densities denoted by small circles.

tributions of cold matter at $x = 0.5$ and 0.3, respectively. We can see from these figures that the phases with rodlike and slablike nuclei, cylindrical and spherical bubbles, in addition to the phase with spherical nuclei are reproduced in both the cases of $x = 0.5$ and 0.3. We here would like to mention the reasons of discrepancies between the present result and the result obtained by Maruyama et al. which says "the nuclear shape may not have these simple symmetries" [23]. One of the most crucial reasons seems to be the difference in treatment of the Coulomb interaction. In the present simulation, we calculate the long range Coulomb interaction in a consistent way using the Ewald method. For the system of interest where the Thomas-Fermi screening length is comparable to or larger than the size of nuclei, this treatment is more adequate than that which inctroduces an artificial cutoff distance as in Ref. [23]. The other crucial reason is the difference in the relaxation time scales τ fm/c; we set $\tau \sim O(10^3 - 10^4)$ in the present work, but Maruyama et al. set $\tau \sim$ several$\times 10^3$ fm/c [27]. In our simulation, we can reproduce the bubble-phases [see (d) and (e) of Figs. 1 and 2] with $\tau \sim 10^3$ fm/c and the nucleus-phases [see (b) and (c) of Figs. 1 and 2] with $\tau \sim O(10^4)$ fm/c. However, the matter in the density region corresponding to a nucleus-phase is quenched in an amorphous-like state when $\tau \lesssim 10^3$ fm/c. In the present work, we take τ much larger than typical time scale $\tau_{\rm th} \sim O(100)$ fm/c for nucleons to thermally diffuse in the distance of $l \sim 10$ fm at $\rho \simeq \rho_0$ and $k_{\rm B}T \simeq 1$ MeV. This temperature is lower than the typical value of the liquid-gas phase transition temperature in the density region of interest, it is thus considered that our results are thermally relaxed in a satisfying level.

Phase diagrams of matter in the ground state are shown in Figs. 3(a) and (b) for $x = 0.5$ and 0.3, respectively. As can be seen from these figures, the obtained phase diagrams basically reproduce the sequence of the energetically favored nuclear shapes predicted by simple discussions [7] which only take account of the Coulomb and surface effects; this prediction is that the nuclear shape changes like sphere → cylinder → slab → cylindrical hole → spherical hole → uniform, with increasing density. Comparing Figs. 3 (a) and (b), we can see that the phase diagram shifts towards the lower density side with decreasing x, which is due to the tendency that the saturation density is lowered as the neutron excess increases. It is remarkable that the density dependence of the nuclear shape, except for spherical nuclei and bubbles, is quite sensitive and phases with intermediate nuclear shapes which are not simple as shown in Figs. 1 and 2 are observed in two density regions: one is between the cylinder phase and the slab phase, the other is between the slab phase and the cylindrical hole phase. We note that these phases are different from coexistence phases with nuclei of simple shapes, which will be referred to as "intermediate phases".

B. QMD Simulations for $x = 0.1$

We have also performed QMD simulations of matter with proton fraction $x = 0.1$ as a more realistic condition for the neutron star matter. In this case, we have to deal with a larger system than in the cases of $x = 0.5$ and 0.3 because enough number of protons for reproducing several nuclei in a simulation box are required to obtain significant results; protons play an important role in generating the long-range order due to their electric charge. We have investigated the neutron-rich matter at $x = 0.1$ with 10976 nucleons, in which 1098 protons and 9878 neutrons are contained. Following basically the same procedure that used for the cases of $x = 0.5$ and 0.3 (see Section III A for detail), we tried to obtain the ground-state matter. However, in the present case, we quickly relax from the initial state at $k_{\rm B}T \sim 20$ MeV to the state at $k_{\rm B}T \sim 10$ MeV, at which matter is still uniform, with a Nosé-Hoover-like thermostat [28, 29] which will be discussed in another paper [25]. After the relaxation at $k_{\rm B}T \sim 10$ MeV for ~ 4000 – 7000 fm/c, we then cool down the system with a relaxation time scale $\tau \sim O(10^4)$ fm/c using the QMD equations of motion with friction terms (17). These simulations are performed by Fujitsu VPP 5000 equipped with MDGRAPE-2.

Some resultant nucleon distributions are shown in Figs. 4 and 5, which correspond to the sphere phase and the cylinder phase, respectively. As can be seen in Fig. 4, dripped neutrons spread over the whole region in the simulation box, which lead to smaller density contrast compared with that for the cases of $x = 0.5$ and 0.3 depicted in Figs. 1 and 2, respectively.

The results obtained for $x = 0.1$ are summarized in the phase diagram shown in Fig. 6. A striking feature is that

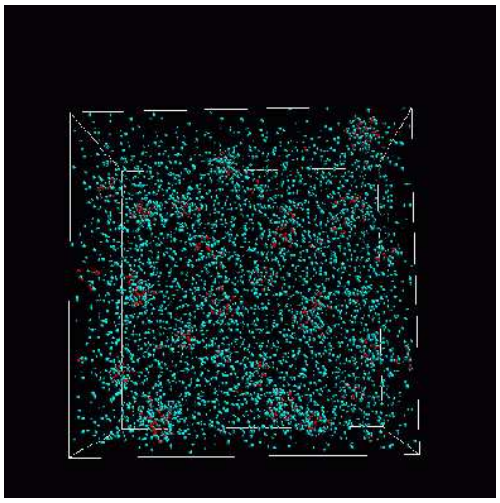

FIG. 4: (Color) The nucleon distribution of sphere phase in cold matter at $x = 0.1$. The nucleon density ρ and the size $L_{\rm box}$ of the simulation box are $\rho = 0.075\rho_0$ and $L_{\rm box} = 96.08$ fm. The red particles represent protons and the green ones represent neutrons.

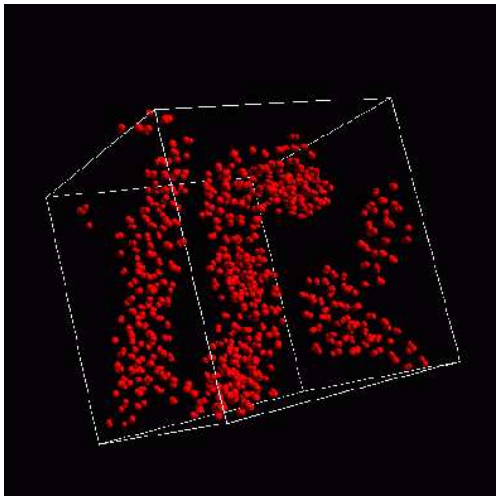

FIG. 5: (Color) The proton distribution of cylinder phase in cold matter at $x = 0.1$. The nucleon density ρ and the size $L_{\rm box}$ of the simulation box are $\rho = 0.2\rho_0$ and $L_{\rm box} = 69.29$ fm. Neutrons which spread over the whole space are not depicted in this figure.

the wide density region from $\sim 0.25\rho_0$ to $\sim 0.525\rho_0$ is occupied by an intermediate phase. The structure of matter seems to change rather continuously from that consists of branching rodlike nuclei connected to each other [obtained in the lower density region of the intermediate phase denoted by (C,U)] to that consists of branching bubbles connected to each other [higher density region of the intermediate phase (C,U)]. However, in the present neutron-rich case, "pasta" phase with slablike nuclei cannot be obtained as far as we have investigated, which will be discussed at the end of the next section. It is also noted that the density at which matter turns into uniform is lower than those in the cases of $x = 0.5$ and 0.3, which is consistent with the tendency that matter becomes the more neutron-rich, the saturation density becomes the lower.

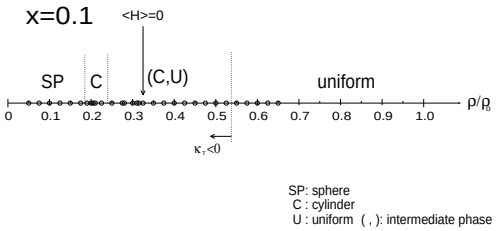

FIG. 6: Phase diagram of cold matter at $x = 0.1$. Matter is unstable against phase separation in the density region shown as $\kappa_{\rm T} < 0$, where $\kappa_{\rm T}$ is the isothermal compressibility. The symbols SP, C and U stand for shapes of nuclear matter region, i.e., sphere, cylinder and uniform, respectively. The density at which the area-averaged mean curvature of nuclear surface is zero is denoted by $\langle H \rangle = 0$. However, slab phase is not observed in our results even at such a density. The parentheses (A,B) show intermediate phases between A-phase and B-phase. They have complicated structures different from those of both A-phase and B-phase. Simulations have been carried out at densities denoted by small circles.

IV. ANALYSIS OF THE STRUCTURE OF MATTER

A. Two-point correlation functions

To analyze the spatial distribution of nucleons, we calculate two-point correlation function ξ_{ii} for nucleon density field $\rho^{(i)}$ ($i = N, p, n$; where N stands for nucleons). ξ_{ii} is here defined as

$$\xi_{ii} = \frac{1}{4\pi}\int d\Omega_{\mathbf{r}}\,\frac{1}{V}\int d^3\mathbf{x}\;\delta_i(\mathbf{x})\delta_i(\mathbf{x}+\mathbf{r}) \qquad (19)$$

$$\equiv \langle \delta_i(\mathbf{x})\delta_i(\mathbf{x}+\mathbf{r})\rangle_{\mathbf{x},\Omega_{\mathbf{r}}}\ , \qquad (20)$$

where $\langle\cdots\rangle_{\mathbf{x},\Omega_{\mathbf{r}}}$ denotes an average over the position $\mathbf{x}$ and the direction of $\mathbf{r}$, and $\delta_i(\mathbf{x})$ is the fluctuation of the density field $\rho^{(i)}(\mathbf{x})$ given by

$$\delta_i(\mathbf{x}) \equiv \frac{\rho^{(i)}(\mathbf{x}) - \overline{\rho^{(i)}}}{\overline{\rho^{(i)}}}\ , \qquad (21)$$

with

$$\overline{\rho^{(i)}} \equiv \frac{N_i}{V}\ . \qquad (22)$$

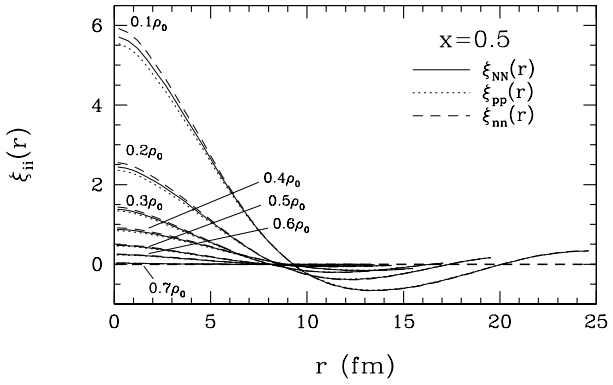

FIG. 7: Two-point correlation functions of density fluctuations calculated for $x = 0.5$. The solid lines show the two-point correlation function for nucleon density distributions; the dotted lines, that for proton density distributions; the dashed lines, that for neutron density distributions.

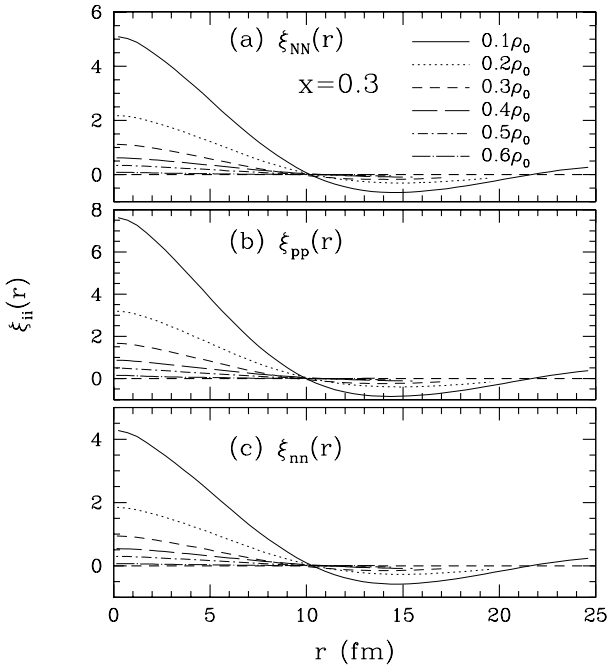

FIG. 8: Two-point correlation functions of density fluctuations calculated for $x = 0.3$; (a) for nucleon density distributions; (b) for proton density distributions; (c) for neutron density distributions.

We construct the nucleon density distribution $\rho^{(i)}(\mathbf{x})$ from a data set of the centers of position of the nucleons by the following procedure. We first set 64^3 (for $x = 0.5$ and 0.3) or 128^3 (for $x = 0.1$) grid points in the simulation box and then distribute particle numbers on each grid point using the cloud-in-cell method (see, e.g., Ref. [30]). Next, we carry out the smoothing procedure in the discrete Fourier space with a Gaussian smoothing function corresponding to the distribution of the wave packet given by Eq. (2). The density distributions $\rho^{(i)}(\mathbf{x}) = \sum_{k=1}^{N} n_k^{(i)} |\phi_k(\mathbf{x})|^2$, where $n_k^{(i)} = 0$ or 1 projects on particle type i, in the discrete real space can be obtained by the inverse Fourier transformation. The Fourier transformations are performed using the FFT algorithm.

The resultant two-point correlation functions $\xi_{NN}(r)$, $\xi_{pp}(r)$ and $\xi_{nn}(r)$ at various densities below $\rho_{\rm m}$ at which matter becomes uniform at zero temperature for $x = 0.5$, 0.3 and 0.1 are plotted in Figs. 7, 8 and 9, respectively. We can see the general tendency, which is common for the different values of x, that the amplitude of $\xi_{ii}(r)$ decreases with increasing the density. It is noted that even though the change in the amplitude of $\xi_{ii}(r)$ is quite noticeable, the smallest zero-point $r = r_0$ of $\xi_{ii}(r)$ takes similar values at various densities especially for $x = 0.5$ and 0.3. This feature means that the typical length scales of the nuclear structures, i.e., the internuclear distance and the nuclear radius, keep comparable at subnuclear densities from $\sim 0.1\rho_0$ to $\rho_{\rm m}$, which is consistent with the results obtained by the previous works (see, e.g., Refs. [8, 9, 10, 13]). This behavior just below $\rho_{\rm m}$ will be discussed further concerning a problem about the properties of the transition to uniform matter.

We also note that a strong attractive force acting between a proton and a neutron leads to the good agreement of the zero-points of ξ_{pp} and ξ_{nn} even for $x = 0.3$ and 0.1 as well as for $x = 0.5$ although the zero-point r_0 of ξ_{nn} is ~ 0.3 fm ($\lesssim 0.5$ fm) larger than that of ξ_{pp} for $x = 0.3$ (0.1) at each density. This shows that the phase of the density fluctuations of protons and neutrons correlate so strongly with each other at zero temperature that they almost coincide.

As can be seen by comparing $\xi_{NN}(r)$ for different values of the proton fraction x, the amplitude decreases and the value of the smallest zero-point r_0 increases with decreasing x. This behavior means that, as matter becomes more neutron-rich, not only the nucleon density distribution gets smoother but also the spatial structure becomes larger.

Let us then examine ξ_{ii} for each value of the proton fraction. For symmetric matter ($x = 0.5$), protons and neutrons are equivalent except for the mass difference and the Coulomb interaction. Therefore, the two-point correlation functions ξ_{NN}, ξ_{pp} and ξ_{nn} are almost the same at larger values of $r \gtrsim r_0$. At smaller values of r, ξ_{pp} is slightly smaller than ξ_{nn} because the repulsive Coulomb interaction among protons tends to reduce the proton density inhomogeneity especially in the smaller scale. For asymmetric matter ($x = 0.3$ and 0.1), on the contrary, the amplitude of ξ_{nn} is much smaller than that of ξ_{pp} due to the dripped neutrons which distribute rather uniformly outside the nuclei.

B. Transition to uniform matter

Let us here examine the properties of the transition from the phase with spherical bubbles to uniform matter

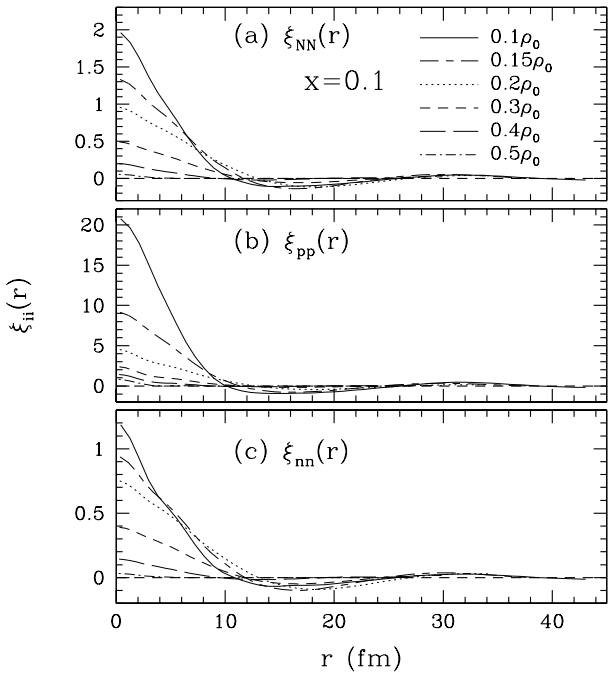

FIG. 9: The same as Fig. 8 for $x = 0.1$.

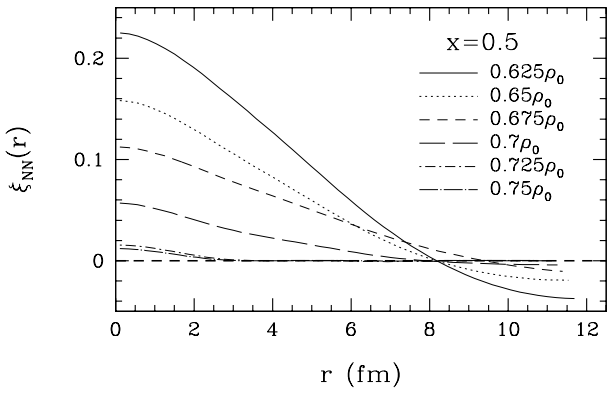

FIG. 10: Two-point correlation function $\xi_{NN}(r)$ of the nucleon density fluctuation. $\xi_{NN}(r)$ is calculated for $x = 0.5$ and for densities around $\rho_{\rm m}$ from $0.625\rho_0$ to $0.75\rho_0$.

for $x = 0.5$. For this purpose, two-point correlation function of the nucleon density fluctuation is useful. In Fig. 10, we thus plot the two-point correlation function of the nucleon density fluctuation $\xi_{NN}(r)$ for several densities around the melting density $\rho_{\rm m}$. To compute $\xi_{NN}(r)$, we use a 1372-nucleon system cooled down until the temperature gets ~ 0.05 MeV by QMD equations of motion (17) with friction terms.

For uniform phase, $\xi_{NN}(r)$ should be zero except for the contribution of short-range correlation. The behavior of $\xi_{NN}(r)$ shows that $\rho_{\rm m}$ lies between $0.7\rho_0$ and $0.725\rho_0$ at $x = 0.5$ [see also Fig. 3(a)] above which long-range correlation disappears. It is noted that the smallest value of $r = r_0$ at which $\xi_{NN}(r) = 0$ keeps around 8 fm even at densities just below $\rho_{\rm m}$. This means that, for $x = 0.5$, the phase with spherical bubbles whose radii are around r_0 suddenly disappear rather than they shrink gradually and the system turns into uniform with increasing the density because the quantity r_0 nearly corresponds to the half wave-length of the inhomogeneous density profile. The discontinuous change in the density profile indicates that the transition between the phase with spherical bubbles and the uniform phase is of first order. This conclusion is also obtained in the previous calculations for which the spatial structure of the nuclear matter region and/or the shape of the density profile are assumed [8, 9, 10, 13, 31]. In the present work, we have confirmed the first order nature by QMD simulations without these assumptions as several authors have done so without the assumptions by the Thomas-Fermi approximation [11, 12].

For the cases of $x = 0.3$ and 0.1, we could not see the significant sign of the first order nature of the transition between the mixed phase and the uniform phase because the amplitude of $\xi_{NN}(r)$ is quite small just below $\rho_{\rm m}$. Further study is necessary to determine the properties of the transition for theses cases of asymmetric matter.

C. Minkowski functionals

To extract the morphological characteristics of the nuclear shape changes and the intermediate phases, we introduce the Minkowski functionals (see, e.g., Ref. [32] and references therein; a concise review is provided by Ref. [33]) as geometrical and topological measures of the nuclear surface. Let us consider a homogeneous body $K \in \mathcal{R}$ in the d-dimensional Eucledian space, where $\mathcal{R}$ is the class of such bodies. Morphological measures are defined as functionals $\varphi : \mathcal{R} \to \mathbf{R}$ which satisfy the following three general properties:

(1) *Motion invariance* : The functional is independent of the position and the direction of the body, i.e.,

$$\varphi(K) = \varphi(gK) \ , \tag{23}$$

where g denotes any translations and rotations.

(2) *Additivity* : The functional of the union of two bodies should behave like a volume. The contribution of the overlapping region should be subtracted , i.e.,

$$\varphi(K_1 \cup K_2) = \varphi(K_1) + \varphi(K_2) - \varphi(K_1 \cap K_2) \ , \tag{24}$$

where $K_1, K_2 \in \mathcal{R}$.

(3) *Continuity* : If the body is approximated with pixels, the functional of the approximate body converges to that of the original body when the pixels get smaller , i.e.,

$$\lim_{n\to\infty} \varphi(K_n) = \varphi(K) \quad \text{as} \quad \lim_{n\to\infty} K_n = K \ , \tag{25}$$

where K is a convex body and $\{K_n\}$ is a sequence of convex bodies.

Hadwiger's theorem in integral geometry states that there are just $d+1$ independent functionals which satisfy the above properties; they are known as Minkowski functionals. In three dimensional space, four Minkowski functionals are related to the volume, the surface area, the integral mean curvature and the Euler characteristic.

In classifying nuclear shapes including those of the intermediate phases obtained in our simulations, the integral mean curvature and the Euler characteristic are useful, which will be discussed later. Both are described by surface integrals of the following local quantities: the mean curvature $H = (\kappa_1 + \kappa_2)/2$ and the Gaussian curvature $G = \kappa_1\kappa_2$, i.e., $\int_{\partial K} H dA$ and $\chi \equiv \frac{1}{2\pi}\int_{\partial K} G dA$, where κ_1 and κ_2 are the principal curvatures and dA is the area element of the surface of the body K. The Euler characteristic χ is a purely topological quantity and is given by

$$\chi = (\text{number of isolated regions}) - (\text{number of tunnels}) + (\text{number of cavities}). \quad (26)$$

Thus $\chi > 0$ for the sphere and the spherical hole phases and the coexistence phase of spheres and cylinders, and $\chi = 0$ for the other ideal "pasta" phases, i.e. the cylinder, the slab and the cylindrical hole phases which consist of infinitely long rods, infinitely extending slabs and infinitely long cylindrical holes, respectively. We introduce the area-averaged mean curvature, $\langle H\rangle \equiv \frac{1}{A}\int H dA$, and the Euler characteristic density, χ/V, as normalized quantities, where V is the volume of the whole space.

1. *Minkowski functionals for $x = 0.5$ and 0.3*

We calculate the normalized Minkowski functionals, i.e., the volume fraction u, the surface area density A/V, the area-averaged mean curvature $\langle H\rangle$ and the Euler characteristic density χ/V for $x = 0.5$ and 0.3 by the following procedure. As described in Subsection IV A, we first construct proton and nucleon density distributions $\rho^{(p)}(\mathbf{r}) = \sum_{k=1}^{N} n_k^{(p)} |\phi_k(\mathbf{r})|^2$ and $\rho(\mathbf{x}) = \sum_{k=1}^{N} |\phi_k(\mathbf{x})|^2$, where $n_k^{(p)} = 0$ or 1 is the isospin projection on the proton state. We set a threshold proton density $\rho_{p,\rm th}$ and then calculate $f(\rho_{p,\rm th}) \equiv V(\rho_{p,\rm th})/A(\rho_{p,\rm th})$, where $V(\rho_{p,\rm th})$ and $A(\rho_{p,\rm th})$ are the volume and the surface area of the regions in which $\rho^{(p)}(\mathbf{r}) \geq \rho_{p,\rm th}$. We find out the value $\rho_{p,\rm th} = \rho^*_{p,\rm th}$ where $\frac{d^2}{d\rho^2_{p,\rm th}} f(\rho^*_{p,\rm th}) = 0$ and define the regions in which $\rho^{(p)}(\mathbf{r}) \geq \rho^*_{p,\rm th}$ as nuclear regions. For spherical nuclei, for example, $\rho^*_{p,\rm th}$ corresponds to a point of inflection of a radial density distribution. In the most phase-separating region, the values of $\rho^*_{\rm th}$ distribute in the range of about $0.07-0.09$ fm^{-3} in the both cases of $x = 0.5$ and 0.3, where $\rho^*_{\rm th}$ is the threshold nucleon density corresponds to $\rho^*_{p,\rm th}$. We then calculate u, A, $\int H dA$ and χ for the identified nuclear surface. We evaluate u by counting the number of pixels at which $\rho^{(p)}(\mathbf{r})$ is higher than $\rho^*_{p,\rm th}$, A by the triangle decomposition method, $\int H dA$ by the algorithm shown in Ref. [32] in conjunction with a calibration by correction of surface area, and χ by the algorithm of Ref. [32] and by that of counting deficit angles [34], which are confirmed that both of them give the same results.

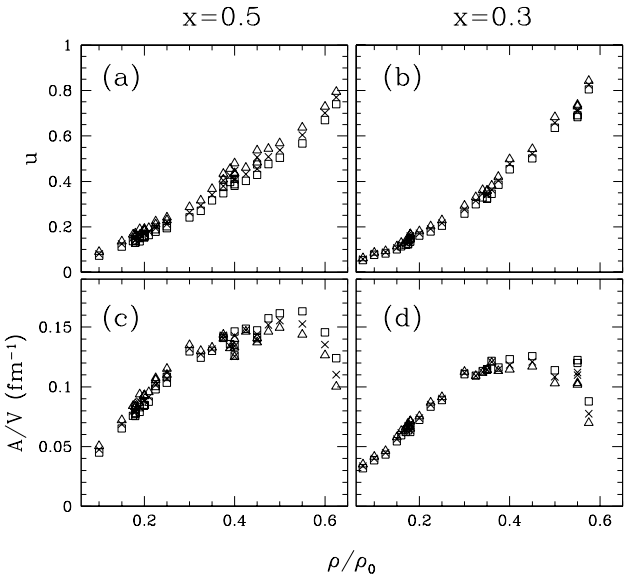

FIG. 11: Density dependence of the volume fraction u and the surface area density A/V of cold matter at $x = 0.5$ (a and c) and $x = 0.3$ (b and d). The crosses show the results for $\rho_{\rm th} = \rho^*_{\rm th}$ and the open triangles and squares show the results for $\rho_{\rm th} = \rho^*_{\rm th} - 0.05\rho_0$ and $\rho^*_{\rm th} + 0.05\rho_0$, respectively.

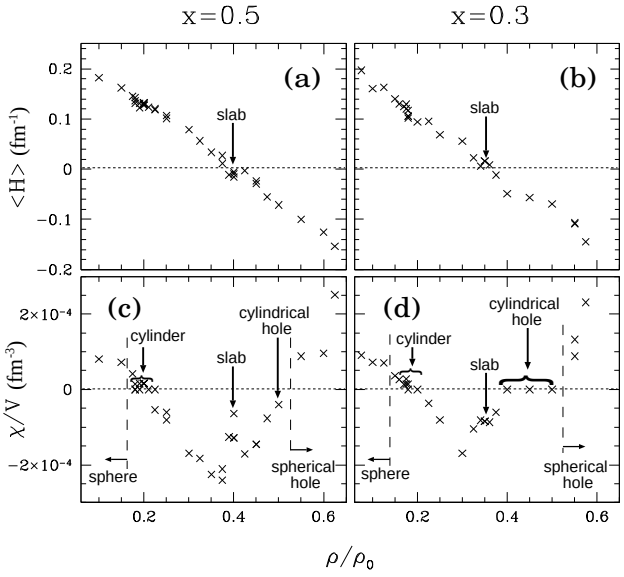

FIG. 12: Density dependence of the area-averaged mean curvature $\langle H\rangle$ and the Euler characteristic density χ/V of cold matter at $x = 0.5$ (a and c) and $x = 0.3$ (b and d).

We have plotted the resultant ρ dependence of u, A/V, $\langle H\rangle$ and χ/V for the isodensity surface of $\rho_{\rm th} = \rho^*_{\rm th}$ in Figs. 11 and 12. In addition to the values of u, A/V and $\langle H\rangle$ for the isodensity surface of $\rho_{\rm th} = \rho^*_{\rm th}$, we have also investigated those for the isodensity surfaces of $\rho_{\rm th} = \rho^*_{\rm th} \pm 0.05\rho_0$ to examine the extent of the uncertainties of these quantities which stem from the arbitrariness in the definition of the nuclear surface. As shown in Fig. 11, these uncertainties are at most $\simeq 0.1$ for u and $\simeq 0.25$ fm^{-1} for A/V. For $\langle H\rangle$, we could not observe remarkable differences from the values for $\rho_{\rm th} = \rho^*_{\rm th}$ (they were smaller than 0.015 fm^{-1}). We could not see these kinds of uncertainties in χ/V, except for the densities near below $\rho_{\rm m}$.

As shown in Fig. 11, the volume fraction u of the nuclear regions increases almost monotonically under $\rho_{\rm m}$ in both cases of $x = 0.5$ and 0.3. This feature reflects the incompressible nature of nuclear matter. It is interesting to see the density dependence of the nuclear surface density A/V because this quantity is directly related to the surface energy density, which is one of the key factors in determining the nuclear shape. Figs. 11(c) and 11(d) show that, as the nucleon density increases, A/V increases at a nearly constant rate until $\rho \sim 0.3\rho_0$, and then its increasing rate becomes rather smaller around the density region of the slab phase, and finally it begins to decrease in the density region of the cylindrical hole phase or the spherical hole phase. This general behavior can be understood from the density dependence of the surface energy density obtained by simple arguments, which only allow for the nuclear surface and the Coulomb effects (see, e.g., Refs. [7, 35]).

We also plot u and A/V for the nucleon density distribution $\rho(\mathbf{r})$ as functions of the threshold density $\rho_{\rm th}$ evaluated at various values of ρ. The results for $x = 0.5$ and 0.3 are shown in Figs. 13 and 14, respectively. Features of nuclear shape changes can be seen in the behavior of the curves of A/V. Peaks in the higher $\rho_{\rm th}$ region are attributed to nucleons in the nuclear matter regions and broad bumps in the lower $\rho_{\rm th}$ region around 0.05 – $0.1\rho_0$ observed for $x = 0.3$ are due to the dripped neutrons outside nuclei. A/V in the intermediate $\rho_{\rm th}$ region in which its slope is nearly constant mainly comes from contribution of nuclear surfaces. As the nucleon density ρ increases, the higher $\rho_{\rm th}$ peak becomes more clear and the position of the center of the peak finally coincides with ρ in the uniform phase. This feature shows that the nuclear matter regions become more uniform with increasing the density. When the dispersion of the internucleon distance is small, large surface area caused by the Gaussian density distribution of each nucleon can be picked up with a single value of $\rho_{\rm th}$. As can be seen in Fig. 14, the lower $\rho_{\rm th}$ bump, in turn, disappears with increasing ρ. This is because, as ρ increases, the dripped neutron gas becomes more inhomogeneous and tends to distribute close to the nuclear surface leading to a lower proton fraction in the nuclear matter regions. It is also noted that, as the nucleon density increases, the slope in

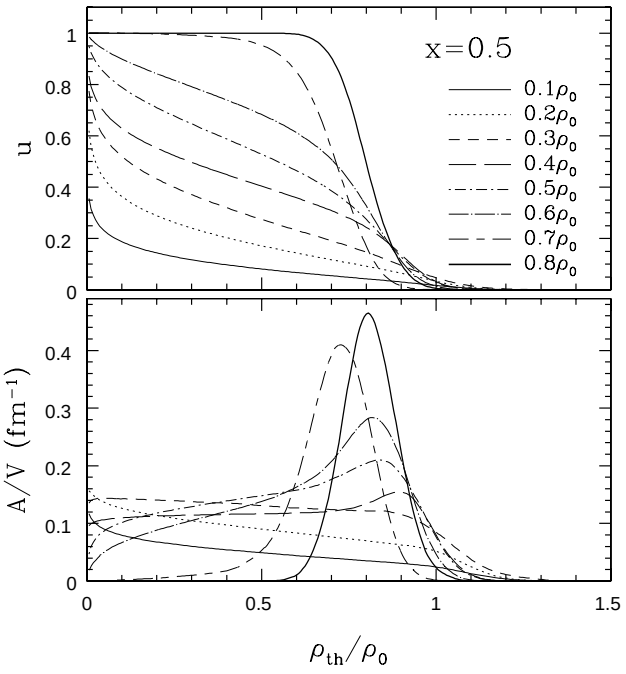

FIG. 13: Volume fraction u (upper panel) and surface area density A/V (lower panel) as functions of the threshold density $\rho_{\rm th}$ calculated for $x = 0.5$ and various nucleon densities ρ.

the intermediate $\rho_{\rm th}$ region changes from negative to positive at the density corresponding to the phase of slablike nuclei ($0.4\rho_0$ for $x = 0.5$ and $0.35\rho_0$ for $x = 0.3$), which is consistent with what is expected from the sign of $\langle H\rangle$ for the nuclear surface [see Figs. 12(a) and 12(b)].

Let us then focus on $\langle H\rangle$ and χ/V to classify the nuclear shape. The behavior of $\langle H\rangle$ shows that it decreases almost monotonically from positive to negative with increasing ρ until the matter turns into uniform. The densities corresponding to $\langle H\rangle \simeq 0$ are about 0.4 and $0.35\rho_0$ for $x = 0.5$ and 0.3, respectively; these values are consistent with the density regions of the phase with slablike nuclei (see Fig. 3). As mentioned previously, χ/V is actually positive in the density regions corresponding to the phases with spherical nuclei, coexistence of spherical and cylindrical nuclei, and spherical holes because of the existence of isolated regions. As for those corresponding to the phases with cylindrical nuclei, planar nuclei and cylindrical holes, $\chi/V \simeq 0$. The fact that the values of χ/V are not exactly zero for nucleon distributions shown as the slab phase in Figs. 1 and 2 reflects the imperfection of these "slabs", which is due to the small nuclear parts connecting the neighboring slabs. However, we can say that the behaviors of χ/V plotted in Figs. 12(c) and 12(d) show that χ/V is negative in the density region of the intermediate phases, even if we take into account the imperfection of the obtained nuclear shapes and the uncertainties of the definition of the nuclear surface. This means that the intermediate phases consist of nuclear surfaces which are saddle-like at each point on average

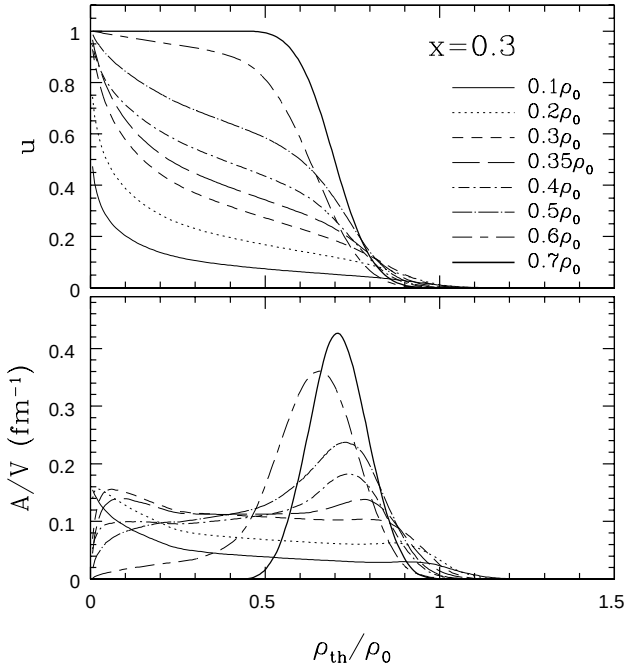

FIG. 14: The same as Fig. 13 for $x = 0.3$.

and they consist of each highly connected nuclear and gas regions due to a lot of tunnels [see Eq. (26)]. Using the quantities $\langle H\rangle$ and χ/V, the sequence of the nuclear shapes with increasing the density can be described as follows: $(\langle H\rangle > 0,\ \chi/V > 0) \rightarrow (\langle H\rangle > 0,\ \chi/V = 0) \rightarrow (\langle H\rangle > 0,\ \chi/V < 0) \rightarrow (\langle H\rangle = 0,\ \chi/V = 0) \rightarrow (\langle H\rangle < 0,\ \chi/V < 0) \rightarrow (\langle H\rangle < 0,\ \chi/V = 0) \rightarrow (\langle H\rangle < 0,\ \chi/V > 0) \rightarrow$ uniform.

Let us now consider the discrepancy from the results of previous works which do not assume nuclear structure [11, 12]; the intermediate phases can not be seen in these works. We can give following two reasons for the discrepancy.

(1) These previous calculations are based on the Thomas-Fermi approximation which can not sufficiently incorporate fluctuations of nucleon distributions. This shortcoming may result in favoring nuclei of smoothed simple shapes than in the real situation.

(2) There is a strong possibility that some highly connected structures which have two or more substructures in a period are neglected in these works because only one structure is contained in a simulation box.

It is not unnatural that the phases with highly connected nuclear and bubble regions are realized as the most energetically stable state [36, 37]. It is considered that, for example, a phase with perforated slablike nuclei, which has negative χ/V, could be more energetically stable than that with extremely thin slablike nuclei. The thin planar nucleus costs surface-surface energy which

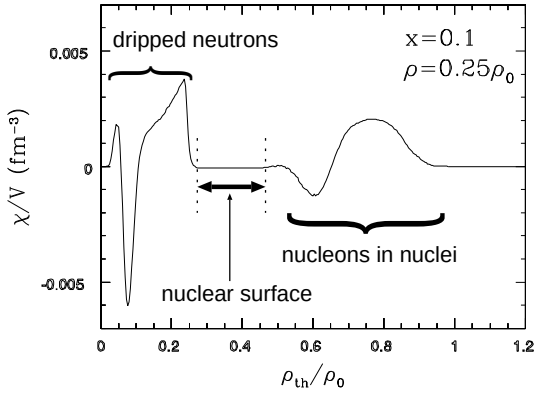

FIG. 15: Euler characteristic density as a function of $\rho_{\rm th}$ calculated for $x = 0.1$ and $\rho = 0.25\rho_0$. The contribution of the nuclear surface can be observed as the plateau region.

stems from the fact that nucleons bound in the nucleus feel its surfaces of both sides. The surface-surface energy brings about an extra energy increase in addition to the contribution of the surface energy. We have to examine the existence of the intermediate phases by more extensive simulations with larger nucleon numbers and with longer relaxation time scales in the future.

2. *Minkowski functionals for $x = 0.1$*

In the case of $x = 0.1$, the criterion for identification of the isodensity surface corresponding to the nuclear surface using the second derivative of $V(\rho_{p,\rm th})/A(\rho_{p,\rm th})$ does not work at higher densities. We thus use another method to calculate the normalized Minkowski functionals of the nuclear surface for $x = 0.1$.

In Fig. 15, we have plotted the $\rho_{\rm th}$ dependence of the Euler characteristic density χ/V at $\rho = 0.25\rho_0$ as an example. We can see that this curve consists of three components: the peaks of the lower $\rho_{\rm th}$ region, the plateau region and the peaks of the higher $\rho_{\rm th}$ region, which are due to dripped neutrons (thus these peaks cannot be observed for $x = 0.5$), nuclear surfaces and nucleons in nuclei, respectively. These components can also be seen at the other values of ρ lower than $\rho_{\rm m}$. However, we have to mention that the higher the density becomes, the smaller the plateau region gets, which means that the density contrast between the dripped neutron gas region and the nuclear matter region becomes obscure. Here, we take the mean values of the normalized Minkowski functionals in the plateau region as those for the nuclear surface, which are plotted as crosses in Fig. 16. The error bars shown in this figure are the standard deviations of these quantities in the plateau region. Consistency between this method and the one using the second derivative of $V(\rho_{p,\rm th})/A(\rho_{p,\rm th})$ has been confirmed for $x = 0.3$.

Fig. 16 shows the resultant normalized Minkowski functionals for the nuclear surface at various values of ρ below $\rho_{\rm m}$. The qualitative behaviors of u and $\langle H\rangle$ for

$x = 0.1$ are the same as those for $x = 0.5$ and 0.3; as ρ increases, u increases and $\langle H \rangle$ decreases (from positive to negative) almost monotonically in the density region of $0.1\rho_0 \lesssim \rho \lesssim \rho_{\rm m}$. However, in the behaviors of A/V and χ/V, qualitative differences can be observed between the present case and the cases of $x = 0.5$ and 0.3. As can be seen in Fig. 16(b), A/V increases almost linearly until just below $\rho_{\rm m}$.

The absence of the phases with cylindrical bubbles and with spherical bubbles in the phase diagram of $x = 0.1$ (Fig. 6) is well characterized by the behavior of χ/V shown in Fig. 16(d). In the cases of $x = 0.5$ and 0.3, χ/V increases from negative to positive with increasing density in the density region higher than that of the slab phase. However, for $x = 0.1$, we cannot observe the tendency that χ/V starts increasing even at just below $\rho_{\rm m}$. As a result, χ/V keeps negative until matter becomes uniform. (Further discussion will be given in Section V.)

Let us then consider the phase with slablike nuclei, which have not been obtained in the simulations for $x = 0.1$. If it were realized by using a longer relaxation time scale, it is expected to be obtained at $\rho \simeq 0.32$ – $0.34\ \rho_0$ according to the behaviors of the $\langle H \rangle$ and χ/V. However, we cannot see any signs from Fig. 16(b) that A/V stops increasing in this density region unlike the behaviors of A/V in the cases of $x = 0.5$ and 0.3. Here, we would like to mention that, according to the Landau-Peierls argument, thermal fluctuations are effective at destroying the long-range order of one-dimensional layered lattice of slablike nuclei rather than that of triangular lattice of rodlike nuclei and of bcc lattice of spherical ones. Thus, the melting temperature of the planar phase would be lower than the other phases, which leads to a longer time scale for formation of the slablike nuclei by the thermal diffusion. Therefore, a further investigation with a longer relaxation time scale is necessary to determine whether or not the phase with slablilke nuclei is really prohibited in such neutron-rich matter in the present model.

In Fig. 17, we have also plotted u and A/V for the density distribution $\rho(\mathbf{r})$ as functions of $\rho_{\rm th}$ like Figs. 13 and 14. In comparison with Fig. 14, the contribution of the dripped neutrons is shown more clearly in this case. We can see that the peak in the lower $\rho_{\rm th}$ region due to the dripped neutrons combines to the peak in the higher $\rho_{\rm th}$ region. This behavior stems from the fact that a part of the dripped neutrons at lower densities are absorbed into nuclear matter region with increasing the density at fixed x; finally, all the neutrons are contained there in the uniform phase. We can also expect from the $\rho_{\rm th}$ dependence of A/V that the phase with slablike nuclei might be obtained around $0.3\rho_0$, where the slope of the plateau region is close to zero.

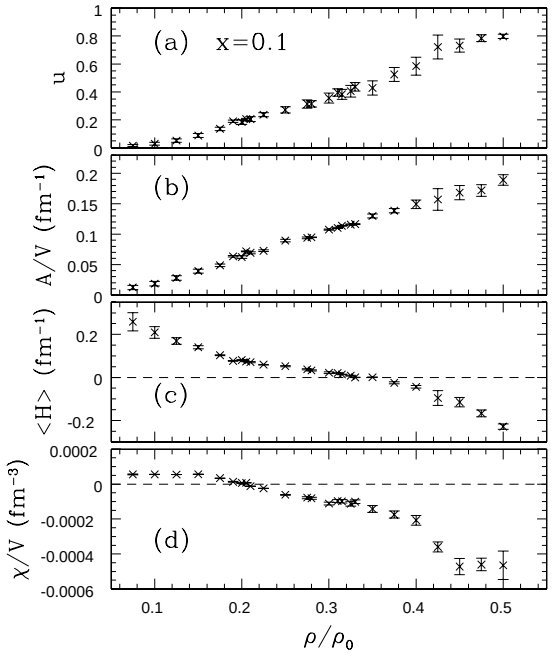

FIG. 16: Density dependence of the normalized Minkowski functionals for cold matter at $x = 0.1$.

V. PROPERTIES OF THE EFFECTIVE NUCLEAR INTERACTION

Let us here examine the effective nuclear interaction used in this work. Structure of matter at subnuclear densities is affected by the properties of neutron-rich nuclei and of the pure neutron gas resulted from the nuclear interaction. Key quantities are the energy per nucleon ϵ_n of the pure neutron matter, the proton chemical potential $\mu_p^{(0)}$ in the pure neutron matter, and the nuclear surface tension $E_{\rm surf}$.

There is a tendency, especially in the case of neutron star matter, that the higher ϵ_n, the density $\rho_{\rm m}$ at which matter becomes uniform is lowered. This is because larger ϵ_n tends to favor uniform nuclear matter without dripped neutron gas regions than mixed phases with dripped neutron gas regions. In the neutron star matter, there is also a tendency that the lower $\mu_p^{(0)}$, the smaller $\rho_{\rm m}$. This is because $-\mu_p^{(0)}$ represents the degree to which the neutron gas outside the nuclei favors the presence of protons in itself. The quantity $E_{\rm surf}$ controls the size of the nuclei and bubbles, and hence the sum of the Coulomb and surface energies. With increasing $E_{\rm surf}$ and so this energy sum, $\rho_{\rm m}$ gets lowered.

It is important to check whether the effective nuclear force given by Eqs. (6)–(12) yields unrealistic values of these quantities or not. If ϵ_n, $|\mu_p^{(0)}|$ and $E_{\rm surf}$ for the present model are unrealistically small in comparison with those for the other models, our results which have reproduced the "pasta" phases might be quite limited for

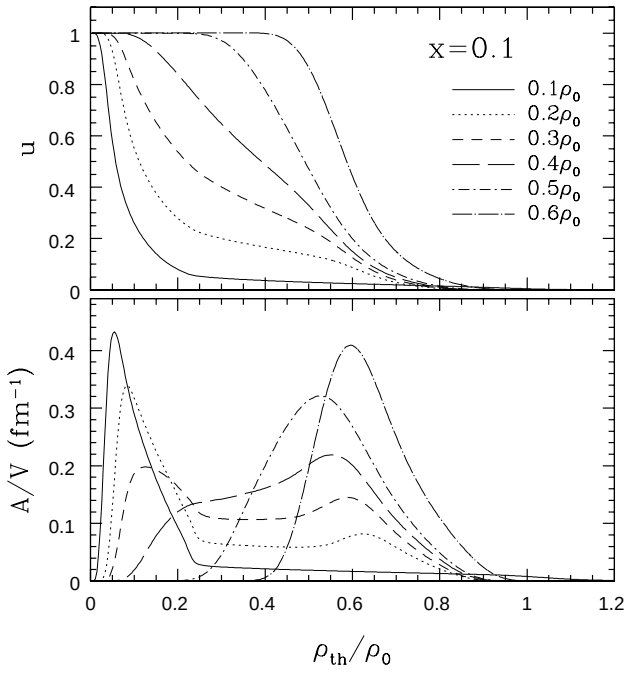

FIG. 17: Volume fraction u (upper panel) and surface area density A/V (lower panel) as functions of the threshold density $\rho_{\rm th}$ calculated for $x = 0.1$ and various nucleon densities ρ.

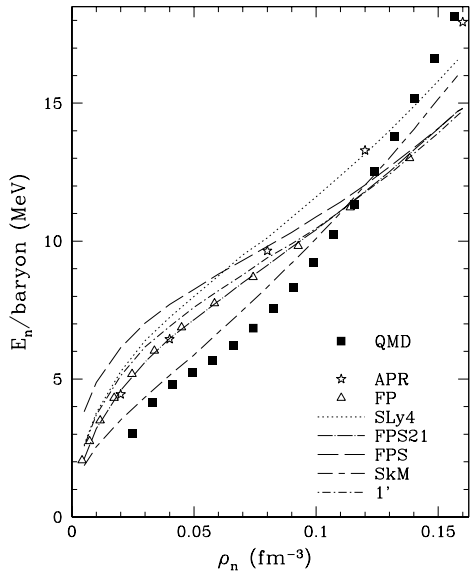

FIG. 18: The neutron density ρ_n dependence of the energy per nucleon ϵ_n of the pure neutron matter. The solid squares show the result of the present QMD model Hamiltonian [23]. The dotted line denoted by SLy4 is the result from Ref. [41] and the broken lines as marked by the other Skyrme interactions (FPS21, 1', FPS and SkM) are the results summarized by Pethick, Ravenhall and Lorenz [40]. The open stars and triangles denote the values obtained by Akmal, Pandharipande and Ravenhall [38], and by Friedman and Pandharipande [39], respectively.

the present model Hamiltonian.

In order to evaluate ϵ_n, we set 1372 neutrons in a simulation box imposed of the periodic boundary condition. This system is cooled down by the QMD equations of motion with friction terms [see Eqs. (17)] until the temperature becomes ~ 1 keV. The resultant values of ϵ_n are plotted in Fig. 18. We note that our results for ρ_n =0.2, 0.6 and 1.0 ρ_0 (the result for $\rho_n = 1.0\rho_0$ is not plotted in Fig. 18) coincide with the results for zero-proton ratio plotted in Fig. 9 of Ref. [23].

The values of ϵ_n for the present model behave like those for the SkM Skyrme interaction especially in the density region of $\rho_n \lesssim 0.13$ fm^{-3}; they are close to the result of the variational chain summation obtained by Akmal, Pandharipande and Ravenhall [38] at $\rho_n \simeq \rho_0$. The steep rise in ϵ_n in the higher neutron density region ($\rho_n \gtrsim 0.1$ fm^{-3}) compared to those obtained from the Hartree-Fock theory using various Skyrme interactions would help neutron-rich matter, which have larger dripped neutron density of $\rho_n \gtrsim 0.1$ fm^{-3}, to be uniform. Therefore, we can say that this behavior of ϵ_n for the present QMD model Hamiltonian suppresses the density region in which the "pasta" phases are the most energetically favorable in neutron star matter and in the case of $x = 0.1$ in the present study. We also note that ϵ_n at lower neutron densities of $\rho_n \lesssim 0.1$ fm^{-3} is relatively small. This, in turn, would lead to increase the density at which matter with lower dripped neutron density (e.g., the case of $x = 0.3$ in the present study) turns into uniform.

Next, we calculate the proton chemical potential $\mu_p^{(0)}$ in the pure neutron matter. We use the cold neutron matter prepared for the above calculation of ϵ_n as an initial condition. We insert a proton into this pure neutron matter, and then minimize the total energy by the frictional relaxation method with fixing the positions and momenta of the other neutrons. The position of the inserted proton is chosen randomly in the simulation box, and its momentum is chosen randomly from $P \leq 30$ MeV/c. We evaluate $\mu_p^{(0)}$ as the difference in the total energy between that before the insertion of the proton and that after the optimization of the position and the momentum of the proton.

In Fig. 19, we plot $\mu_p^{(0)}$ for the present model Hamiltonian. As can be seen from this figure, the result for the present model Hamiltonian generally reproduce the data of the other results obtained from the Hartree-Fock theory using the various Skyrme interactions at densities $\rho \lesssim 0.1$ fm^{-3}. At lower densities of $\rho \lesssim 0.025$ fm^{-3}, errors are quite large and data scatter significantly. This is because density fluctuations in pure neutron matter obtained by QMD would be unrealistically large at such low densities due to the fixed width of the wave packets in this model. However, it is noted that even in such a density region, our data are generally consistent with the

other results mentioned above.

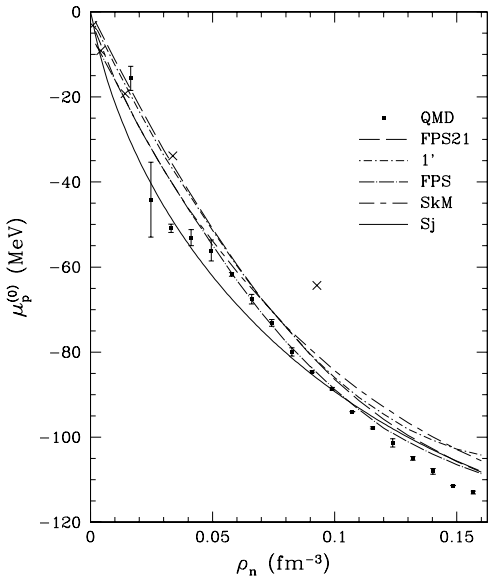

FIG. 19: The neutron density dependence of the proton chemical potential $\mu_p^{(0)}$ in the pure neutron matter. The solid squares show the result of the present QMD Hamiltonian [23]. The broken lines as marked by the Skyrme interactions (FPS21, 1', FPS and SkM) are the results summarized by Pethick, Ravenhall and Lorenz [40], and the solid line is the result of Sjöberg [42]. The crosses denote the values obtained by Siemens and Pandharipande [43].

Finally, we turn to the surface tension, which affects energetically favorable nuclear shape most directly among the three quantities discussed here. We have calculated $E_{\rm surf}$ from the energy change induced by the change in the area of planar nuclear matter. We use nucleon gas with proton fractions $x = 0.1$, 0.2, 0.3 and 0.5 composed of 1372 nucleons. In the calculation of $E_{\rm surf}$, the Coulomb interaction is excluded.

In order to prepare slablike nuclear matter, we first cool down the above nucleon gas from $k_{\rm B}T \sim 20$ MeV to ~ 0.2 MeV using Eqs. (17) in a shallow trapping harmonic potential

$$V(z) = \frac{k}{2} z^2 \ , \tag{27}$$

where $k = 0.01$ MeV fm^{-2}. The simulation box here is imposed of the periodic boundary condition in the x- and y-directions, and is imposed of the open boundary condition in the z-direction. The box size $L_{x,y}$ in the x- and y-directions is set 20.26 fm.

When the temperature reaches ~ 0.2 MeV, we remove the trapping potential and, except for the case with $x = 0.5$, we change the boundary condition in the z-direction from open to periodic. The box size in the z-direction L_z is chosen so as to at least all nucleons dripped outside the nuclear matter region can be contained in the box: $L_z = 92.32$ fm ($x = 0.1$), 79.12 fm ($x = 0.2$), and 82.85 fm ($x = 0.3$). After we relax the system for ~ 7000 fm/c, we prepare three kinds of samples: one is nothing changed (sample 1) and the others have the area of the xy side of the simulation box increased (decreased) by 1 % with the total volume of the box kept constant [sample 2 (sample 3)]. We further cool them down until $k_{\rm B}T \sim 0.1$ keV. The resultant nucleon density profiles for the sample 1 of $x = 0.1$ projected on the z-axis is shown in Fig. 20. As can be seen from this figure, $L_z = 92.32$ fm is much larger than the thickness of the slab $d \simeq 20$ fm, and thus the volume of the dripped neutron gas region is almost the same among the three kinds of samples because the volume change in the nuclear matter region is negligible. It is also noted that d is much larger than the surface thickness $d_{\rm surf} \simeq 5$ fm, which ensures that the surfaces at both sides of the slab are separated well. Therefore, we can say that the energy difference between the sample 2 and 3 is just due to the difference in the surface area of the planar nuclear matter. Following the spirit of Ravenhall, Bennett and Pethick (hereafter RBP) [44] and by using the sample 1, we define the proton fraction $x_{\rm in}$ in the nuclear matter region as an averaged value for the region of the width of $\simeq 5$ fm in the central part of the slab, where the proton and neutron density profiles ripple around constant values.

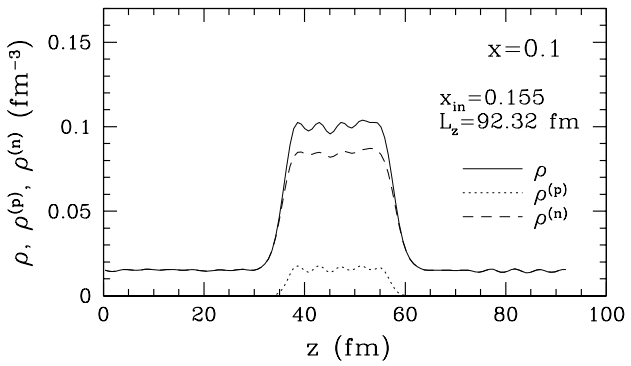

FIG. 20: The nucleon density profiles projected on the z-axis for the sample 1 of $x = 0.1$. (The z-coordinate is shifted.)

We extract $E_{\rm surf}$ from the total energy E_2 of the sample 2 and E_3 of the sample 3 as follows:

$$E_{\rm surf} = \frac{E_2 - E_3}{2(S_2 - S_3)} \ , \tag{28}$$

where S_2 (S_3) is the area of the xy side of the sample 2 (sample 3) given by $20.26^2 \times 1.01$ fm^2 ($20.26^2 \times 0.99$ fm^2). The factor 2 in the denominator represents, of course, the contribution of the two sides of the planar nuclear matter. As shown in Fig. 21, all the results plotted in this figure almost coincide with each other at $x_{\rm in} = 0.5$, where uncertainty in the nuclear surface tension is rather small. These results deviate significantly at lower $x_{\rm in}$, and the values of $E_{\rm surf}$ of the present calculation lie between those obtained by Baym, Bethe and Pethick (hereafter BBP)

[2] and by RBP [44], which is based on the Hartree-Fock calculation using a Skyrme interaction, at $x_{\rm in} \sim 0.15 - 0.35$. Thus we can say that, in comparison with the result by RBP taken to be standard here, the contribution of $E_{\rm surf}$ of the present QMD model tends to favor uniform nuclear matter rather than the inhomogeneous "pasta" phases for lower $x_{\rm in}$ of $\lesssim 3.5$.

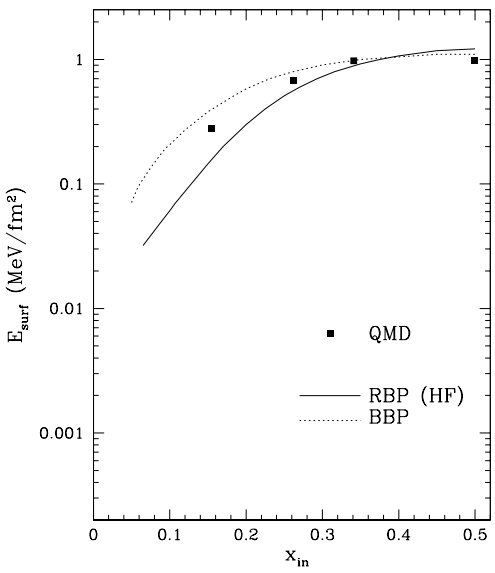

FIG. 21: The nuclear surface energy per unit area (the surface tension) versus the proton fraction $x_{\rm in}$ in the nuclear matter region. The solid squares are the values of the present QMD Hamiltonian [23], the solid curve is the RBP result from their Hartree-Fock calculations [44], and the dotted curve is the BBP result [2].

Now let us discuss the fact that the intermediate phases with a negative value of χ/V are obtained instead of the bubble phases in a wide density region for $x = 0.1$. In considering this problem, we should note the general tendency that $|\mu_p^{(0)}|$ increases and $E_{\rm surf}$ decreases as matter becomes neutron-rich (see Figs. 19 and 21). The density dependence of A/V monotonically increases until $\rho_{\rm m}$ as shown in Fig. 16 would partly stem from the small value of $E_{\rm surf}$. The apparently lower melting density $\rho_{\rm m}$ in this case than in the cases of $x = 0.5$ and 0.3, even though $E_{\rm surf}$ is small, is due to a large $|\mu_p^{(0)}|$, which increases typically of order 10 MeV as ρ_n increases. The small $E_{\rm surf}$ and the large $|\mu_p^{(0)}|$ in neutron-rich matter would help nuclear matter regions and neutron gas regions mix each other at the cost of small surface energy below $\rho_{\rm m}$. As a result, the structures with a negative χ/V could be favored. According to Fig. 19, the quantity $\mu_p^{(0)}$ obtained for the present model Hamiltonian is consistent with those for the other Skyrme-Hartree-Fock calculations in the relevant region of $\rho_n \lesssim 0.08$ fm^{-3}. It is thus possible that a result which shows the structure of matter changes from negative χ/V to uniform without undergoing "swiss cheese" structure will be obtained by another calculation for neutron-rich matter using some framework without assuming nuclear shape.

In closing this subsection, we summarize the consequences of the resultant ϵ_n, $\mu_p^{(0)}$ and $E_{\rm surf}$ for the present QMD Hamiltonian.

1. For symmetric matter ($x = x_{\rm in} = 0.5$)

   According to $E_{\rm surf}$ at $x_{\rm in} = 0.5$, the present model is consistent with the other results, and is an appropriate effective interaction for the study of the "pasta" phases at $x = 0.5$.

2. For neutron-rich cases

   For neutron-rich cases such as $x \sim 0.1$, in which the dripped neutron density ρ_n grows $\gtrsim 0.1$ fm^{-3} just before matter turns into uniform, the present QMD model can be taken as a conservative one in reproducing the "pasta" phases. Its ϵ_n, $\mu_p^{(0)}$ and $E_{\rm surf}$ act to suppress the density region of the "pasta" phases compared to other Skyrme-Hartree-Fock results.

3. For intermediate cases

   At intermediate proton fraction of $x \sim 0.3$, ϵ_n of the present model acts to favor the inhomogeneous "pasta"phases rather than the uniform phase and $E_{\rm surf}$ acts in the opposite way in comparison with other Skyrme-Hartree-Fock results.

VI. ASTROPHYSICAL DISCUSSIONS

Here we would like to discuss astrophysical consequences of our results. Pethick and Potekhin have pointed out that elastic properties of "pasta" phases with rodlike and slablike nuclei are similar to those of liquid crystals, which stems from the similarity in the geometrical structures [15]. It can also be said that the intermediate phases observed in the present work are "spongelike" (or "rubberlike" for $\langle H \rangle < 0$) phases because they have both highly connected nuclear and bubble regions shown as $\chi/V < 0$. The elastic properties of the spongelike intermediate phases are qualitatively different from those of the liquid-crystal-like "pasta" phases because the former ones do not have any directions in which the restoring force does not act; while the latter ones have. Our results imply that the intermediate phases occupy a significant fraction of the density region in which nonspherical nuclei can be seen (see Figs. 3 and 6). According to Figs. 3 and 6, we expect that the maximum elastic energy that can be stored in the neutron star crust and supernova inner core is higher than that in the case where all nonspherical nuclei have simple "pasta" structures. Besides, the cylinder and the slab phases, which are liquid-crystal-like, lie between the spongelike intermediate phases or the crystalline solidlike phase, and the releasing of the strain energy would, in consequence, concentrate in the domain

of these liquid-crystal-like phases. The above effects of the intermediate phases should be taken into account in considering the crust dynamics of starquakes and hydrodynamics of the core collapse, etc. if these phases exist in neutron star matter and supernova matter. In the context of pulsar glitch phenomena, the effects of the spongelike nuclei on the pinning rate and the creep velocity of superfluid neutron vortices also have yet to be investigated.

For neutrino cooling of neutron stars, some version of the direct URCA process which is suggested by Lorenz et al. [8], that this might be allowed in the "pasta" phases, would be suppressed in the intermediate phases. This is due to the fact that the proton spectrum at the Fermi surface is no longer continuous in the spongelike nuclei. An important topic which we would like to mention is about the effects of the intermediate phases on neutrino trapping in supernova cores. The nuclear parts connect over a wide region which is much larger than that characterized by the typical neutrino wave length ~ 20 fm. Thus the neutrino scattering processes are no longer coherent in contrast to the case of the spherical nuclei, and this may, in consequence, reduce the diffusion time scale of neutrinos as in the case of "pasta" phases with simple structures. This reduction softens the supernova matter and would thus act to enhance the amount of the released gravitational energy. It would be interesting to estimate the neutrino opacity of the spongelike phases and the "pasta" phases.

Finally, we would like to mention the thermal fluctuations with long wavelengths leading to displacements of "pasta" nuclei, which cannot be incorporated into the simulations using a finite-size box. Even if we succeed in reproducing the phase with slablike nuclei in neutron-rich matter in the future study, we should remind the above effect of thermal fluctuations to consider the real situation of matter in inner crusts of neutron stars. Following the discussions in Refs. [9, 10, 35] by a liquid-drop model, it is likely that the extension of slablike nuclei is limited to a finite length scale of $\sim O(10^2 - 10^3)$ fm in the temperature regions typical for neutron star crusts and supernova cores.

VII. SUMMARY AND CONCLUSION

We have performed QMD simulations for matter with fixed proton fractions $x = 0.5$, 0.3 and 0.1 at various densities below the normal nuclear density. Our calculations without any assumptions on the nuclear shape demonstrate that the "pasta" phases with rodlike nuclei, with slablike nuclei, with cylindrical bubbles and with spherical bubbles can be formed dynamically from hot uniform matter within the time scale of $\tau \sim O(10^3 - 10^4)$ fm/c in the proton-rich cases of $x = 0.5$ and 0.3. We also demonstrate that the "pasta" phase with cylindrical nuclei can be formed dynamically within the time scale of $\tau \sim O(10^4)$ fm/c for the neutron-rich case of $x = 0.1$. Our results imply the existence of at least the phase with cylindrical nuclei in neutron star crusts because they cool down keeping the local thermal equilibrium after proto-neutron stars are formed and their cooling time scale, which is macroscopic one, is much larger than the relaxation time scale of our simulations.

In addition to these "pasta" phases with simple structures, our results obtained here also suggest the existence of intermediate phases which have complicated nuclear shapes. We have systematically analyzed the structure of matter with two-point correlation functions and with morphological measures "Minkowski functionals", and have demonstrated how structure changes with increasing density. Making use of a topological quantity called Euler characteristic, which is one of the Minkowski functionals, it has been found that the intermediate phases can be characterized as those with negative Euler characteristic. This means that the intermediate phases have "spongelike" (or "rubberlike" for $\langle H \rangle < 0$) structures which have both highly connected nuclear and bubble regions. The elastic properties of the spongelike intermediate phases are qualitatively different from those of the liquid-crystal-like "pasta" phases.

We have also investigated the properties of the effective QMD interaction used in the present work in order to examine the validity of our results. Important quantities which affect the structure of matter are the energy per nucleon ϵ_n of the pure neutron matter, the proton chemical potential $\mu_p^{(0)}$ in pure neutron matter and the nuclear surface tension $E_{\rm surf}$. The resultant these quantities show that the present QMD interaction has generally reasonable properties at subnuclear densities among other nuclear interactions. It is thus concluded that our results are not exceptional ones in terms of nuclear forces.

Our results which suggest the existence of the highly connected intermediate phases as well as the simple "pasta" phases provide a vivid picture that matter in neutron star inner crusts and supernova inner cores has a variety of material phases. The stellar region which we have tried to understand throughout this paper is relatively tiny, but there has quite rich properties which stem from the fancy structures of dense matter.

Acknowledgments

G. W. is grateful to T. Maruyama, K. Iida, A. Tohsaki, H. Horiuchi, K. Oyamatsu, H. Takemoto, K. Niita, S. Chikazumi, I. Kayo, C. Hikage, T. Buchert, N. Itoh and K. Kotake for helpful discussions and comments. G. W. also appreciate J. Lee for checking the manuscript. This work was supported in part by the Junior Research Associate Program in RIKEN through Research Grant No. J130026 and by Grants-in-Aid for Scientific Research provided by the Ministry of Education, Culture, Sports, Science and Technology through Research Grant (S) No. 14102004, No. 14079202 and No. 14-7939.

APPENDIX A: THE EWALD SUM FOR PARTICLES WITH A GAUSSIAN CHARGE DISTRIBUTION

In calculating a long-range interaction, such as the Coulomb interaction, it is necessary to sum up all contributions of particles at a sufficiently far distance. The Ewald sum is a familiar technique for efficiently computing the long-range contributions in a system with the periodic boundary condition (see, e.g., Refs. [26, 45]; recent mathematically careful discussion relating to the conditionally convergence of the Coulomb energy can be seen, e.g., in Ref. [46]). The basic idea of the Ewald sum is that the contributions of particles in a long distance in real space can be calculated as contributions in the neighborhood in Fourier space: the contributions of particles in a short distance is summed up in real space and those of particles in a long distance is summed up in Fourier space.

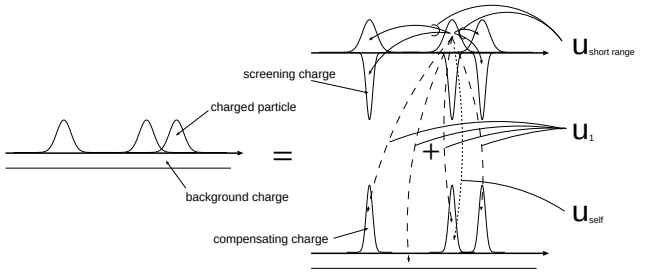

FIG. 22: Schematic picture of charge distribution in the Ewald sum for particles with a Gaussian charge distribution.

Let us consider a system consisting of charged particles which have a Gaussian charge distribution and a uniform background charge which cancels the total charge of charged particles. These N particles are assumed to be in a cubic simulation box with volume $V = L_{\rm box}^3$ which is imposed by the periodic boundary condition.

If every particle i with total charge Z_i is surrounded by a Gaussian charge distribution with total charge $-Z_i$, the electrostatic interaction of particle i turns into a screened short-range interaction. Thus the total Coulomb energy $\mathcal{U}_{\rm Coul}$ of this system can be decomposed into as follows (see Fig. 23):

$$\mathcal{U}_{\rm Coul} = \mathcal{U}_{\text{short range}} + \mathcal{U}_1 - \mathcal{U}_{\rm self} \ , \tag{A1}$$

where $\mathcal{U}_{\text{short range}}$ is the sum of the Coulomb energy between an each unscreened charged particle i and the other charged particles with screening charges, $\mathcal{U}_1$ is that between an each unscreened charged particle i and compensating charges which cancels the screening Gaussian charges, and $\mathcal{U}_{\rm self}$ is the sum of spurious self interactions between an each charged particle i and its compensating charge i.

Charge densities of the real charged particles $\rho(\mathbf{r})$ and of the screening charges $\rho_s(\mathbf{r})$ can be written as

$$\begin{aligned}\rho(\mathbf{r}) &= \sum_{\mathbf{n}}\sum_{i=1}^{N} Z_i \left(\frac{a}{\pi}\right)^{3/2} e^{-a|\mathbf{r}-(\mathbf{r}_i+L_{\rm box}\mathbf{n})|^2} \\ &\equiv \sum_{\mathbf{n}}\sum_{i=1}^{N} \rho_{(\mathbf{n},i)}(\mathbf{r}), \end{aligned} \tag{A2}$$

$$\begin{aligned}\rho_s(\mathbf{r}) &= -\sum_{\mathbf{n}}\sum_{i=1}^{N} Z_i \left(\frac{\alpha_{\rm Ewald}}{\pi}\right)^{3/2} e^{-\alpha_{\rm Ewald}|\mathbf{r}-(\mathbf{r}_i+L_{\rm box}\mathbf{n})|^2} \\ &\equiv \sum_{\mathbf{n}}\sum_{i=1}^{N} \rho_{s,(\mathbf{n},i)}(\mathbf{r}), \end{aligned} \tag{A3}$$

where a and $\alpha_{\rm Ewald}$ are the reciprocals of the widths of charge distributions for a charged particle and a screening charge, respectively, and $\mathbf{n}$ denotes a position vector of a periodic image normalized by $L_{\rm box}$. Thus a distribution of screened charges $\rho_{\rm screened}$ is

$$\rho_{\rm screened}(\mathbf{r}) \equiv \rho(\mathbf{r}) + \rho_s(\mathbf{r}) \ . \tag{A4}$$

The electrostatic potential $\phi_{\text{short range}}(\mathbf{r})$ due to $\rho_{\rm screened}(\mathbf{r})$ can be obtained as

$$\phi_{\text{short range}}(\mathbf{r}) = \sum_{\mathbf{n}}\sum_{i=1}^{N} Z_i \left\{ -\frac{\mathrm{erfc}(\sqrt{a}\ |\mathbf{r}-(\mathbf{r}_i+L_{\rm box}\mathbf{n})|)}{|\mathbf{r}-(\mathbf{r}_i+L_{\rm box}\mathbf{n})|} + \frac{\mathrm{erfc}(\sqrt{\alpha_{\rm Ewald}}\ |\mathbf{r}-(\mathbf{r}_i+L_{\rm box}\mathbf{n})|)}{|\mathbf{r}-(\mathbf{r}_i+L_{\rm box}\mathbf{n})|} \right\} + \ C \ , \tag{A5}$$

because a solution of the Poisson equation

$$-\frac{1}{r}\frac{d^2}{dr^2}(r\phi(r)) = 4\pi \left[Z \left(\frac{a}{\pi}\right)^{3/2} e^{-ar^2} \right] \tag{A6}$$

is

$$\phi(r) = Z\frac{\mathrm{erf}(\sqrt{a}\ r)}{r} + \text{const.} \ , \tag{A7}$$

where $\mathrm{erf}(x)$ and $\mathrm{erfc}(x)$ are the error function and the complementary error function, respectively, and they are defined as $\mathrm{erf}(x) \equiv \frac{2}{\sqrt{\pi}}\int_0^x \exp(-s^2)\ ds$ and $\mathrm{erfc}(x) \equiv 1 - \mathrm{erf}(x)$. Here, we determine the constant C so that the average value of $\phi_{\text{short range}}$ in the simulation box V

be zero:

$$\int_V \phi_{\text{short range}}(\mathbf{r})\ d^3\mathbf{r} = \sum_{i=1}^{N} Z_i \left(-\frac{\pi}{a} + \frac{\pi}{\alpha_{\text{Ewald}}}\right) + CV = 0\ . \quad \text{(A8)}$$

Thus, $\phi_{\text{short range}}(\mathbf{r})$ leads to

$$\phi_{\text{short range}}(\mathbf{r}) = \sum_{\mathbf{n}}\sum_{i=1}^{N} Z_i \left\{-\frac{\text{erfc}(\sqrt{a}\ |\mathbf{r}-(\mathbf{r}_i+L_{\text{box}}\mathbf{n})|)}{|\mathbf{r}-(\mathbf{r}_i+L_{\text{box}}\mathbf{n})|} + \frac{\text{erfc}(\sqrt{\alpha_{\text{Ewald}}}\ |\mathbf{r}-(\mathbf{r}_i+L_{\text{box}}\mathbf{n})|)}{|\mathbf{r}-(\mathbf{r}_i+L_{\text{box}}\mathbf{n})|}\right\} - \left(-\frac{\pi}{a} + \frac{\pi}{\alpha_{\text{Ewald}}}\right)\rho_{\text{avr}}\ , \quad \text{(A9)}$$

where the average charge density ρ_{avr} of the charged particles is defined as

$$\rho_{\text{avr}} \equiv \sum_{i=1}^{N} \frac{Z_i}{V}\ . \quad \text{(A10)}$$

The total Coulomb energy $\mathcal{U}_{\text{short range}}$ between an each unscreened real charged particle i and the other charged particles with a screening charge can be calculated as

$$\begin{aligned}\mathcal{U}_{\text{short range}} &= \frac{1}{2}\sum_{i=1}^{N}\Bigg\{\int d^3\mathbf{r}\int d^3\mathbf{r}'\rho_{(\mathbf{n}=0,i)}(\mathbf{r}) \\ &\quad \sum_{\mathbf{n}'}{\sum_{j}}' Z_j \left\{-\frac{\text{erfc}(\sqrt{a}\ |\mathbf{r}-(\mathbf{r}_j+L_{\text{box}}\mathbf{n})|)}{|\mathbf{r}-(\mathbf{r}_j+L_{\text{box}}\mathbf{n})|} + \frac{\text{erfc}(\sqrt{\alpha_{\text{Ewald}}}\ |\mathbf{r}-(\mathbf{r}_j+L_{\text{box}}\mathbf{n})|)}{|\mathbf{r}-(\mathbf{r}_j+L_{\text{box}}\mathbf{n})|}\right\} \\ &\quad -\left(-\frac{\pi}{a}+\frac{\pi}{\alpha_{\text{Ewald}}}\right)\rho_{\text{avr}}\Bigg\} \\ &= \frac{1}{2}\sum_{\mathbf{n}}{\sum_{i,j}}' \frac{Z_i Z_j}{|\mathbf{r}_i-(\mathbf{r}_j+L_{\text{box}}\mathbf{n})|}\left\{\text{erfc}\left(\sqrt{\frac{a\ \alpha_{\text{Ewald}}}{a+\alpha_{\text{Ewald}}}}\ |\mathbf{r}_i-(\mathbf{r}_j+L_{\text{box}}\mathbf{n})|\right)\right. \\ &\quad \left.-\text{erfc}\left(\sqrt{\frac{a}{2}}\ |\mathbf{r}_i-(\mathbf{r}_j+L_{\text{box}}\mathbf{n})|\right)\right\} - \frac{V}{2}\left(-\frac{\pi}{a}+\frac{\pi}{\alpha_{\text{Ewald}}}\right)\rho_{\text{avr}}^2\ , \end{aligned} \quad \text{(A11)}$$

where the primes on the summations mean the terms $i = j$ at $\mathbf{n} = 0$ are excluded.

Next, we calculate $\mathcal{U}_1$, which is the sum of the Coulomb energy between an unscreened charged particle i and a charge density $\rho_1(\mathbf{r})$ which consists of the compensating charges and the background charge:

$$\begin{aligned}\rho_1(\mathbf{r}) &= -\rho_s(\mathbf{r}) - \rho_{\text{avr}} \\ &= \sum_{\mathbf{n}}\sum_{j=1}^{N} Z_j \left(\frac{\alpha_{\text{Ewald}}}{\pi}\right)^{3/2} e^{-\alpha_{\text{Ewald}}|\mathbf{r}-(\mathbf{r}_j+L_{\text{box}}\mathbf{n})|^2} \\ &\quad -\rho_{\text{avr}}\ . \end{aligned} \quad \text{(A12)}$$

Fourier transforming the charge distribution $\rho_1(\mathbf{r})$ yields

$$\begin{aligned}\rho_1(\mathbf{k}) &= \frac{1}{V}\int_V d^3\mathbf{r} e^{-i\mathbf{k}\cdot\mathbf{r}}\rho_1(\mathbf{r}) \\ &= \frac{1}{V}\sum_{j=1}^{N} Z_j e^{-i\mathbf{k}\cdot\mathbf{r}_j} e^{-\frac{k^2}{4\alpha_{\text{Ewald}}}} - \rho_{\text{avr}}\ \delta_{\mathbf{k}} \end{aligned} \quad \text{(A13)}$$

Using $\rho_1(\mathbf{k})$ and the Poisson equation ($\nabla^2\phi_1(\mathbf{r}) = -4\pi\rho_1(\mathbf{r})$) in the Fourier form

$$k^2\phi_1(\mathbf{k}) = 4\pi\rho_1(\mathbf{k})\ , \quad \text{(A14)}$$

we can at once obtain the electrostatic potential ϕ_1 due

to the charge density ρ_1:

$$\phi_1(\mathbf{r}) = \sum_{\mathbf{k}} \phi_1(\mathbf{k}) e^{i\mathbf{k}\cdot\mathbf{r}} = \frac{1}{V}\sum_{\mathbf{k}\neq 0}\sum_{j=1}^{N} \frac{4\pi Z_j}{k^2}\, e^{i\mathbf{k}\cdot(\mathbf{r}-\mathbf{r}_j)} e^{-\frac{k^2}{4\alpha_{\rm Ewald}}} \ . \quad \text{(A15)}$$

The term with $\mathbf{k} = 0$ is canceled due to charge neutrality. Thus the Coulomb energy $\mathcal{U}_1$ is given by

$$\mathcal{U}_1 = \frac{1}{2}\sum_{i=1}^{N}\int d^3\mathbf{r} Z_i \left(\frac{a}{\pi}\right)^{3/2} e^{-a|\mathbf{r}-\mathbf{r}_i|^2}\phi_1(\mathbf{r}) = \frac{1}{2}\sum_{\mathbf{k}\neq 0}\sum_{i,j}\frac{4\pi Z_i Z_j}{Vk^2}\, e^{i\mathbf{k}\cdot(\mathbf{r}_i-\mathbf{r}_j)} \times e^{-\frac{k^2}{4}\left(\frac{1}{\alpha_{\rm Ewald}}+\frac{1}{a}\right)} \ . \quad \text{(A16)}$$

We have to subtract a sum of spurious self interactions $\mathcal{U}_{{\rm self},i}$ between a charged particle i and its compensating charge from $\mathcal{U}_1$. According to Eq. (A7), an electrostatic potential $\phi_{\rm Gauss}$ due to a Gaussian compensating charge is $\phi_{\rm Gauss}({\rm r}) = Z_i\ {\rm erf}(\sqrt{\alpha_{\rm Ewald}}\ r)/r$, thus the self interaction of particle i reads to

$$\mathcal{U}_{{\rm self},i} \equiv \int Z_i \left(\frac{a}{\pi}\right)^{3/2} e^{-ar^2}\phi_{\rm Gauss}(r)\ d^3\mathbf{r} = 2\left(\frac{a}{\pi}\right)^{1/2} Z_i^2 \sqrt{\frac{\alpha_{\rm Ewald}}{a+\alpha_{\rm Ewald}}} \ , \quad \text{(A17)}$$

and hence,

$$\mathcal{U}_{\rm self} = \frac{1}{2}\sum_{i=1}^{N}\mathcal{U}_{{\rm self},i} = \frac{1}{\sqrt{\pi}}\sqrt{\frac{a\ \alpha_{\rm Ewald}}{a+\alpha_{\rm Ewald}}}\sum_{i=1}^{N} Z_i^2 \ . \quad \text{(A18)}$$

Finally, the total Coulomb energy can be calculated by Eqs. (A1), (A11), (A16) and (A18). The positive background charge does not appear explicitly because the average value of $\phi_{\text{short range}}$ within the simulation box is set to be zero.

The total Coulomb energy per particle $e_{\rm Coul}$ and the x component of the Coulomb force $f_{1,x}$ acting on a particle for various values of $\alpha_{\rm Ewald}$ are plotted in Fig. 23. In this calculation, we use 1024 positive charged particles (protons) distributed randomly in a simulation box of $L_{\rm box} = 39.59$ fm (i.e. $\rho_p = 0.1\rho_0$), which is imposed of the periodic boundary condition. Figs. 23 (a) and 23 (b) show the results for point charges and for Gaussian charge distributions, respectively, which are calculated for the same configuration of the particle positions $\{\mathbf{r}_i\}$. The width of the Gaussian charge distributions is set to be $a = 1/2L$ with $L = 2.1$ fm^2, which corresponds to the width of the wave packets in the QMD model used in this work.

We note that there are plateau regions of $e_{\rm Coul}$ and $f_{1,x}$ whose values do not depend on $\alpha_{\rm Ewald}$. These constant values give results to be obtained. We note that the range

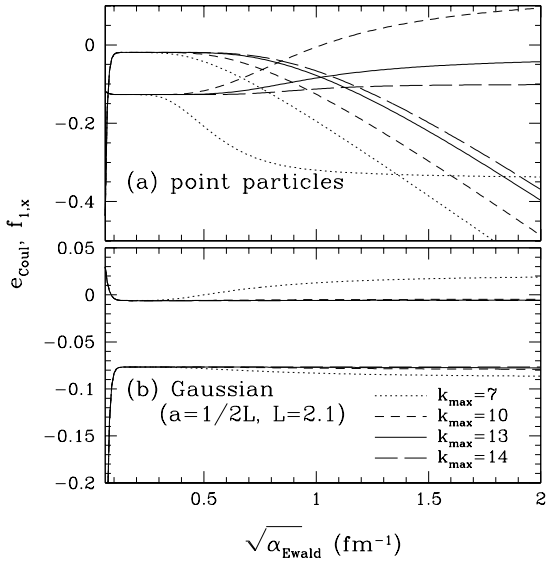

FIG. 23: The total Coulomb energy per particle $e_{\rm Coul}$ (in units of MeV) and the x component of the Coulomb force $f_{1,x}$ (in units of MeV/fm) acting on a particle obtained from Eqs. (A1), (A11), (A16) and (A18) as a function of $\sqrt{\alpha_{\rm Ewald}}$. We use 1024 protons distributed randomly in a box of $L_{\rm box} = 39.59$ fm (i.e. $\rho_p = 0.1\rho_0$). The results shown in (a) and (b) are calculated for the same configuration of particle positions $\{\mathbf{r}_i\}$ but for different values of the width a of the Gaussian distribution; (a) $a = 0$ (point charge) and (b) $a = 1/2L$ with $L = 2.1$ fm^2.

of $\sqrt{\alpha_{\rm Ewald}}$ of the plateau regions become larger with increasing $k_{\rm max}$, where $k_{\rm max}$ is the cutoff radius in the unit of $2\pi/L_{\rm box}$ for the summation in Fourier space. As can be seen from Fig. 23, $\alpha_{\rm Ewald}$ dependences of $e_{\rm Coul}$ and $f_{1,x}$ for the present QMD model with a finite width of the Gaussian charge distributions are weaker than those for the point charges. These features are also confirmed for different proton number densities of 0.2 and 0.3 ρ_0. In our simulations, $\alpha_{\rm Ewald}$ is set 13 or 14, which are considered to be large enough to calculate the total Coulomb energy per particle in accuracy less than $O(1)$ keV, which is the typical value of the energy difference between successive "pasta" phases in neutron star matter obtained by previous works.

[1] H.A. Bethe, G. Borner and K. Sato, Astron. Astrophys. **7**, 279 (1970).

[2] G. Baym, H. A. Bethe and C. J. Pethick, Nucl. Phys.

A175, 225 (1971).
[3] K. Sato, Prog. Theor. Phys. **54**, 1325 (1975).
[4] H. A. Bethe, Rev. Mod. Phys. **62**, 801 (1990).
[5] C. J. Pethick and D. G. Ravenhall, Annu. Rev. Nucl. Part. Sci. **45**, 429 (1995).
[6] D. G. Ravenhall, C. J. Pethick and J. R. Wilson, Phys. Rev. Lett. **50**, 2066 (1983).
[7] M. Hashimoto, H. Seki and M. Yamada, Prog. Theor. Phys. **71**, 320 (1984).
[8] C.P. Lorenz, D.G. Ravenhall and C.J. Pethick, Phys. Rev. Lett. **70**, 379 (1993).
[9] G. Watanabe, K. Iida and K. Sato, Nucl. Phys. **A676**, 455 (2000); Erratum, Nucl. Phys. A (in press).
[10] G. Watanabe, K. Iida and K. Sato, Nucl. Phys. **A687**, 512 (2001); Erratum, Nucl. Phys. A (in press).
[11] R. D. Williams and S. E. Koonin, Nucl. Phys. **A435**, 844 (1985).
[12] M. Lassaut, H. Flocard, P. Bonche, P.H. Heenen and E. Suraud, Astron. Astrophys. **183**, L3 (1987).
[13] K. Oyamatsu, Nucl. Phys. **A561**, 431 (1993).
[14] P. B. Jones, Mon. Not. R. Astron. Soc. **296**, 217 (1998); Mon. Not. R. Astron. Soc. **306**, 327 (1998); Phys. Rev. Lett. **83**, 3589 (1999).
[15] C. J. Pethick and A.Y. Potekhin, Phys. Lett. **B427**, 7 (1998).
[16] C. J. Horowitz, Phys. Rev. D **55** (1997) 4577.
[17] K. Iida, G. Watanabe and K. Sato, Prog. Theor. Phys. **106**, 551 (2001).
[18] J. Aichelin and H. Stöcker, Phys. Lett. **B176**, 14 (1986).
[19] H. Feldmeier and J. Schnack, Rev. Mod. Phys. **72**, 655 (2000).
[20] G. Watanabe, K. Sato, K. Yasuoka and T. Ebisuzaki, Phys. Rev. C **66**, 012801(R) (2002).
[21] H. Feldmeier, Nucl. Phys. **A515**, 147 (1990).
[22] A. Ono, H. Horiuchi, T. Maruyama and A. Ohnishi, Prog. Theor. Phys. **87**, 1185 (1992); Phys. Rev. Lett. **68**, 2898 (1992).
[23] T. Maruyama, K. Niita, K. Oyamatsu, T. Maruyama, S. Chiba and A. Iwamoto, Phys. Rev. C **57**, 655 (1998).
[24] In some cases, the Nosé-Hoover-like thermostat which will be described in another paper [25] is also used. In the present study, employment of this thermostat is almost limited in a higher temperature region where matter is completely uniform.
[25] G. Watanabe, K. Sato, K. Yasuoka and T. Ebisuzaki, in preparation.
[26] M. P. Allen and D. J. Tildesley, *Computer Simulation of Liquids* (Clarendon, Oxford, 1987).
[27] T. Maruyama, private communication.
[28] S. Nosé, J. Chem. Phys. **81**, 511 (1984).
[29] W. G. Hoover, Phys. Rev. A **31**, 1695 (1985).
[30] R. W. Hockney and J. W. Eastwood, *Computer Simulation Using Particles* (IOP Publishing, Bristol, 1988).
[31] R. Ogasawara and K. Sato, Prog. Theor. Phys. **68**, 222 (1982).
[32] K. Michielsen and H. De Raedt, Phys. Rep. **347**, 461 (2001).
[33] J. Schmalzing, S. Engineer, T. Buchert, V. Sahni and S. Shandarin, (1996) unpublished.
[34] J. R. Gott III, A. L. Melott and M. Dickinson, Astrophys. J. **306**, 341 (1986); D. H. Weinberg, Publ. Astron. Soc. Pacific **100**, 1373 (1988).
[35] G. Watanabe, PhD thesis, Univ. of Tokyo (2003).
[36] Existence of some phase with a complicated structure is also suggested by P. Magierski and P. H. Heenen, Phys. Rev. C **65**, 045804 (2002). They focus on shell effects of dripped neutrons.
[37] Non-integral values of the "dimensionality" d in the early work done by Ravenhall et al. [6] also suggest the possibilty of complicated nuclear shapes.
[38] A. Akmal, V. R. Pandharipande and D. G. Ravenhall, Phys. Rev. C **58**, 1804 (1998).
[39] B. Friedman and V. R. Pandharipande, Nucl. Phys. **A361**, 501 (1981).
[40] C. J. Pethick, D. G. Ravenhall and C. P. Lorenz, Nucl. Phys. **A584**, 675 (1995).
[41] F. Douchin and P. Haensel, Phys. Lett. **B485**, 107 (2000).
[42] O. Sjöberg, Nucl. Phys. **A222**, 161 (1974).
[43] P. J. Siemens and V. R. Pandharipande, Nucl. Phys. **A173**, 561 (1971).
[44] D. G. Ravenhall, C. D. Bennett and C. J. Pethick, Phys. Rev. Lett. **28**, 978 (1972).
[45] M. P. Tosi, in: F. Seitz and D. Turnbull (Eds.), *Solid State Physics: Advances in Research and Applications* (Academic Press, New York, 1964) p. 1.
[46] H. Takemoto, T. Ohyama and A. Tohsaki, Prog. Theor. Phys. **109**, 563 (2003).